

Centimeter-wave continuum radiation from the ρ Ophiuchi molecular cloud

Simon Casassus^{1*}, Clive Dickinson², Kieran Cleary³, Roberta Paladini²,
Mireya Etxaluze^{4,5}, Tanya Lim⁵, Glenn J. White^{4,5}, Michael Burton⁶,
Balt Indermuehle⁶, Otmar Stahl⁷, Patrick Roche⁸

¹ *Departamento de Astronomía, Universidad de Chile, Casilla 36-D, Santiago, Chile*

² *Infrared Processing and Analysis Center, California Institute of Technology, M/S 220-6, 1200 E. California Blvd., Pasadena, CA 91125.*

³ *Chajnantor Observatory, M/S 105-24, California Institute of Technology, Pasadena, CA 91125*

⁴ *Department of Physics and Astronomy, The Open University, Milton Keynes MK7 6AA, UK*

⁵ *The Rutherford Appleton Laboratory, Didcot, Oxfordshire OX11 0QX, UK.*

⁶ *School of Physics, University of New South Wales, Sydney NSW 2052, Australia*

⁷ *ZAH, Landessternwarte Königstuhl, 69117 Heidelberg, Germany*

⁸ *Astrophysics, Oxford University, DWB, Keble Road, Oxford OX1 3RH, UK*

ABSTRACT

The ρ Oph molecular cloud is undergoing intermediate-mass star formation. UV radiation from its hottest young stars heats and dissociates exposed layers, but does not ionize hydrogen. Only faint radiation from the Rayleigh-Jeans tail of ~ 10 – 100 K dust is expected at wavelengths longwards of ~ 3 mm. Yet Cosmic Background Imager (CBI) observations reveal that the ρ Oph W photo-dissociation region (PDR) is surprisingly bright at centimetre wavelengths. We searched for interpretations consistent with the *WMAP* radio spectrum, new *ISO-LWS* parallel mode images and archival *Spitzer* data. Dust-related emission mechanisms at 1 cm, as proposed by Draine & Lazarian, are a possibility. But a magnetic enhancement of the grain opacity at 1 cm is inconsistent with the morphology of the dust column maps N_d and the lack of detected polarization. Spinning dust, or electric-dipole radiation from spinning very small grains (VSGs), comfortably explains the radio spectrum, although not the conspicuous absence from the CBI data of the infrared circumstellar nebulae around the B-type stars S 1 and SR 3. Allowing for VSG depletion can marginally reconcile spinning dust with the data. As an alternative interpretation we consider the continuum from residual charges in ρ Oph W, where most of carbon should be photoionised by the close binary HD147889 (B2IV, B3IV). Electron densities of $\sim 10^2$ cm⁻³, or H-nucleus densities $n_H > 10^6$ cm⁻³, are required to interpret ρ Oph W as the C II Strömgren sphere of HD147889. However the observed steep and positive low-frequency spectral index would then require optically thick emission from an hitherto unobserved ensemble of dense clumps or sheets with a filling factor $\sim 10^{-4}$ and $n_H \sim 10^7$ cm⁻³.

Key words: radiation mechanisms: general, radio continuum: general ISM, sub-millimetre, ISM: clouds,

1 INTRODUCTION

The subtraction of Galactic foregrounds in experiments designed to map the cosmic microwave background requires the examination of the emission mechanisms at work in the interstellar medium (ISM). An anomalous component of continuum emission was discovered in the direction of

Galactic cirrus clouds (Leitch et al. 1997), so defined by their H I 21 cm and far-IR contours (e.g. Boulanger & Perault 1988). The LDN 1622 dark cloud (Lynds Dark Nebula, Lynds 1962) was found to be bright at cm-wavelengths, where no known emission mechanisms were expected (Finkbeiner et al. 2002; Finkbeiner 2004; Casassus et al. 2006). At the time of writing LDN 1622 is the only dark cloud known to radiate at cm-wavelengths.

* E-mail: simon@das.uchile.cl (SC)

What is the nature of the cm-wave emitters? Do the

arXiv:0809.3965v1 [astro-ph] 23 Sep 2008

dark clouds and the cirrus clouds radiate by the same emission mechanisms? Draine & Lazarian (1998a,b) proposed electric dipole radiation from polarized very small dust grains (VSGs) spinning at GHz frequencies, or spinning dust. Draine & Lazarian (1999) also suggested that ‘magnetic dust’, or magnetic dipole emission due to thermal fluctuations in the magnetization of ferromagnetic grains, could produce detectable cm-wave emission. However, a finite charge density exists in atomic and molecular clouds; a small part of the neutral material is ionised by exposure to pervasive cosmic rays or soft-UV photons (e.g. Tielens 2005). As an alternative to spinning dust, could the residual charges radiate at the observed levels?

Prototypical and well studied local clouds can give information on the environments giving rise to cm-wave radiation. The ρ Oph molecular cloud (e.g. Encrenaz 1974; Young et al. 2006), at a distance $D = 135 \pm 15$ pc (parallax distance to HD147889, Habart et al. 2003), lies in the Gould Belt of the closest molecular complexes. ρ Oph is undergoing intermediate-mass star formation - the most massive of its young stars is HD147889, which we show here to be a close pre-main-sequence B2, B3 binary, not hot enough to form a conspicuous region of ionized-hydrogen (H II region). A description of the region can be found in Fig. 4 of Young et al. (2006).

Here we present the first resolved images at cm-wavelengths of the ρ Oph main cloud, LDN 1688. We describe our observations in Section 2, as well as auxiliary data in Sec. 3, including unpublished *ISO*-LWS parallel mode data. We proceed to summarise the available imaging and spectroscopic data in Sec. 4. The dust emission from ρ Oph W and the contribution of spinning or magnetic dust at cm-wavelengths are studied critically in Sec. 5. We also propose in Sec. 6 an alternative emission mechanism for the 31 GHz emission based on the C I continuum from a cold plasma. In Sec. 7 we analyse the non-detection of the radio recombination line system in ρ Oph W. We discuss our findings in Sec. 8 in terms of the C II Strömgren spheres around the early type stars that are interacting with the ρ Oph cloud, before concluding in Sec. 9.

2 CBI OBSERVATIONS

The 31 GHz image of ρ Oph that motivates this work is shown in Fig. 1. It was reconstructed from the CBI visibilities using a maximum entropy method. In this section we give details on the CBI observations and image reconstruction.

2.1 Total intensity

The Cosmic Background Imager (CBI Padin et al. 2002) is a planar interferometer array with 13 antennas, each 0.9 m in diameter, mounted on a 6 m tracking platform. The CBI receivers operate in 10 frequency channels covering 26–36 GHz. It is located in Llano de Chajnantor, Atacama, Chile. With a uniform-weight synthesised beam of ~ 6 arcmin and a primary beam of 45.2 arcmin full-width at half maximum at 31 GHz, the CBI is well suited to image clouds ~ 20 –30 arcmin in total extent. The CBI primary beam (CBI PB hereafter) encompasses most of LDN 1688.

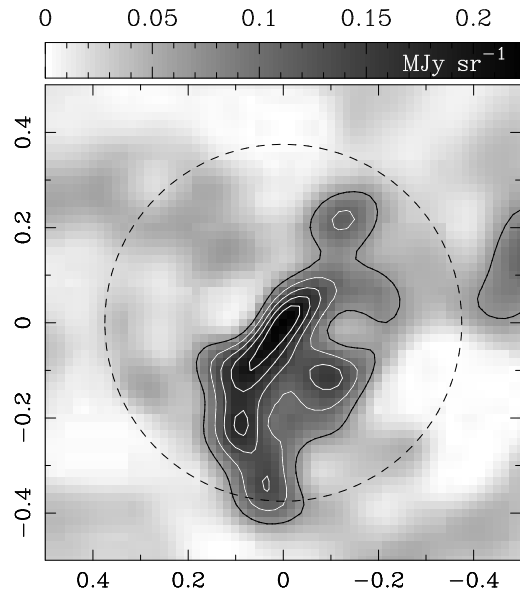


Figure 1. MEM model of the CBI 31 GHz visibilities. x - and y -axis show offset RA and DEC from ρ Oph W (J2000 16h25m57s, -24d20m50s), in degrees of arc. The contour levels are at 0.067, 0.107, 0.140, 0.170 and 0.197, in MJy sr^{-1} . The dashed-circle follows the half-maximum level of the CBI primary beam (CBI PB hereafter).

During three nights of July 2004 and April 2005 we acquired 31 GHz visibilities in a single pointing on the ρ Oph W photo-dissociation region (PDR, Habart et al. 2003), with the CBI in its compact configuration, for a total of ~ 12000 s on-source. Baseline length ranged between 100λ and 400λ , corresponding to spatial scales of 34.4 arcmin and 8.6 arcmin, respectively. Cancellation of ground and Moon contamination was obtained by differencing with a leading reference field at the same declination but offset in hour angle by 10 m, the duration of the on-source integration.

2.2 Image reconstruction

We produced the MEM model in Fig. 1 by minimising the model functional $L = \chi^2 - \lambda S$, where the expression for χ^2 is given by Eq. A1 in Casassus et al. (2006), and with $S = -\sum_i I_i \log(I_i/M_i)$, where $\{I_i\}_{i=1}^N$ is the model image and M_i is an image prior. The sum extends over the number of independent data points, which is $f = 31680$ (two for each of 15840 complex visibilities). In this case we chose a regularizing parameter $\lambda = 200$, and square model images with 256^2 square pixels, each 1 arcmin on a side. The optimization converged in 20 iterations. The image prior was constructed from a combination of the IRAC 4 image at $8 \mu\text{m}$ (see Sec. 3.2) and WMAP Ka at 33 GHz (see Sec. 3.5). More details on image reconstruction are given in Sec. A.

2.3 Polarization

ρ Oph was also observed by the CBI in polarization during four nights in August, September and October 2004. Details of the polarization calibration and data reduction pro-

cedures can be found in Readhead et al. (2004); Cartwright et al. (2005); Dickinson et al. (2006); Casassus et al. (2007). Data from all nights were combined together. They were mapped with DIFMAP using natural weights and optimal noise weighting. A polarized intensity map was created using AIPS COMB and POLC option to correct for the noise bias. The noise on the Q and U maps is about 9 mJy beam⁻¹. The beam is 9.5×8.3 arcmin².

No obvious polarization signal is visible in the polarized intensity map, and is consistent with an rms noise of 12 mJy beam⁻¹. Using the same weighting scheme (same visibilities and synthesized beam), the peak total-intensity is 752 mJy beam⁻¹.

At peak total intensity, the 1 σ polarization limit is 12 / 752 = 1.6%, or a 3 σ upper limit of 4.8%. In the weaker regions of ρ Oph W, where the total-intensity drops to typically 100 – 200 mJy beam⁻¹, the polarization limit increases to \sim 12 / 150 = 8%, or 24% at 3 σ .

For the integrated flux density over a 45 arcmin diameter aperture, the polarization limit has to be calculated using a primary-beam corrected map which multiplies up both the signal and the noise. This was done, making a noise corrected polarized intensity map assuming a noise level of 45 mJy beam⁻¹ (average over the field). The rms in this image is 57 mJy beam⁻¹. So the integrated polarization limit is 1.0% at 3 σ .

3 AUXILIARY DATA

3.1 ISO parallel mode data

The *ISO* Long Wavelength Spectrograph parallel mode survey¹ covered most of LDN 1688 in 10 bands ranging from 46 μ m to 178 μ m. The full set of *ISO* images is shown in Fig. 2. The broad wavelength coverage of the *ISO* data allows dust mass and extinction estimates (see Sec. 5.1). Especially relevant to this work is the 178 μ m image, which is used in the discussion of magnetic dust in Sec. 5.2.

The parallel mode data were obtained when another *ISO* instrument was operating with total sky coverage of about 1%. The processing of parallel data was the same as for the primary mode data. Engineering conversions were applied to obtain the photocurrents. Once the photocurrents were obtained the dark current was removed. The calibration of the detector responsivity relies on a simple ratio between the response to the illuminators found at the time of a particular observation and that used as a reference. Parallel mode maps were produced at ten detector wavelengths and are generated by combining different rasters. Several data reduction tools were developed in IDL and these form the LWS parallel interactive analysis package that can be found at: <http://jackal.bnsc.rl.ac.uk/isouk/lws/software/software.html>.

We have compared the *ISO* data at 102.26 μ m with the *IRAS* 100 μ m survey (Wheelock et al. 1991). It is noteworthy that the *ISO* 102.26 μ m intensities below 1000 MJy sr⁻¹ are typically 27 % higher than *IRAS* 100 μ m, 40 % higher above 1000 MJy sr⁻¹. This is in agreement with the results of Chan

(2001) and García Lario (2001). According to the *IRAS* explanatory supplement, the gain and non-linearity of the detectors is a function of source extension, which could be the source of the intensity-dependent discrepancy between *ISO* and *IRAS*.

3.2 Spitzer archival data

The *IRAC* data span the range 3.6 to 8 μ m with four distinct bands (centered at 3.6, 4.5, 5.6 and 8 μ m) and an angular resolution of 2''. Longer wavelengths, namely 24, 70 and 160 μ m, are covered by *MIPS* data, with angular resolutions of 9, 18 and 40'' respectively. Both the *IRAC* and *MIPS* data considered in the present paper come from the *c2d* *Spitzer* Legacy Survey². The *MIPS* data are described by Padgett et al. (2008), in connection with the young stellar population of ρ Oph.

Archival *Spitzer* *IRS* data were obtained for positions near the early-type stars S 1, SR 3 and a region of the filament. For SR3 and the filament (Berné et al. 2007), the data were taken in spectral mapping mode using the high resolution (SH and LH) modules of *IRS*. In this mode, the spectrograph slit is moved before each integration in order to cover the region of interest. The Basic Calibrated Data (BCD) files from the archive were produced using the S15 pipeline by the *Spitzer* Science Centre. The spectral cubes were assembled from the BCD files using the CUBISM software package (Smith et al. 2004). Spectra were extracted from the spectral cubes using an aperture which was covered by both SH and LH modules, as shown in Fig. 3. For S 1, the data were taken in low-resolution (SL) staring mode and were also produced using the S15 pipeline. The original target was a young stellar object (J162630-242258, Barsony et al. 1997) located behind the circumstellar nebula about S 1. We performed a full-slit extraction of SL1 with the target in the SL1 slit and also with the target in SL2. This resulted in SL1 spectra at two distinct positions in the S 1 nebulosity, which we call ‘S 1’ and ‘S 1off’, as also shown in Fig. 3. The position ‘S 1off’ is located at the northern edge of the IR nebulosity surrounding the early-type star S 1.

3.3 FEROS and UNSW-MOPS observations

3.3.1 FEROS

HD147889 is the main source of excitation in ρ Oph W so an accurate measurements of its spectral type is necessary. HD147889 is catalogued in SIMBAD as a single B2III/IV star (Houck & Smith-Moore 1988). However Hafner & Meyer (1995) reported that HD147889 is a close binary. The spectral types they quote are B2 for both components, and luminosity class IV-V. Unfortunately Hafner & Meyer (1995) do not give details on their atmospheric models. Given the importance of HD147889 for ρ Oph W we undertook new echelle observations and up-to-date atmospheric modelling.

In order to precisely determine the UV field impinging on ρ Oph W we acquired echelle spectroscopy of HD147889 during 2 contiguous nights in May 2008 (ESO programme

² see the *Spitzer* Science Center press release,

¹ http://www.iso.vilspa.esa.esmanualsHANDBOOK/lws_hbnode1.html <http://www.spitzer.caltech.edu/Media/releases/ssc2008-03/release.shtml>

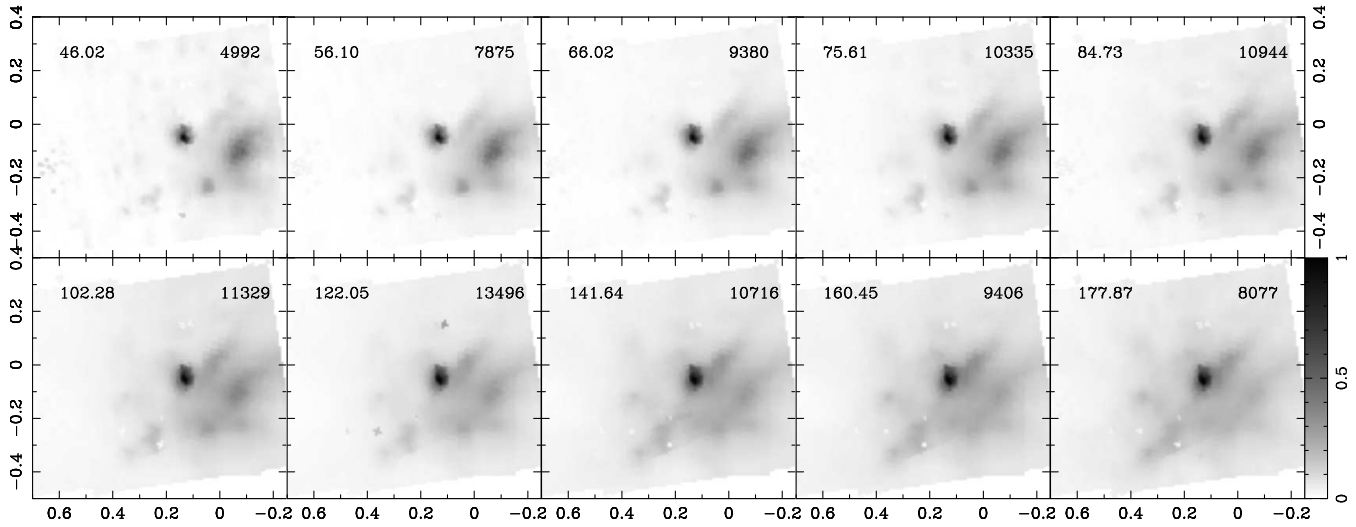


Figure 2. The *ISO*-LWS parallel mode data on ρ Oph. x - and y -axis show offset RA and DEC from ρ Oph W, in degrees. The centre wavelength in microns of the LWS channels are indicated on the upper-left of each image. The intensities in MJy sr^{-1} have been scaled by the amount indicated on the upper-right of each image.

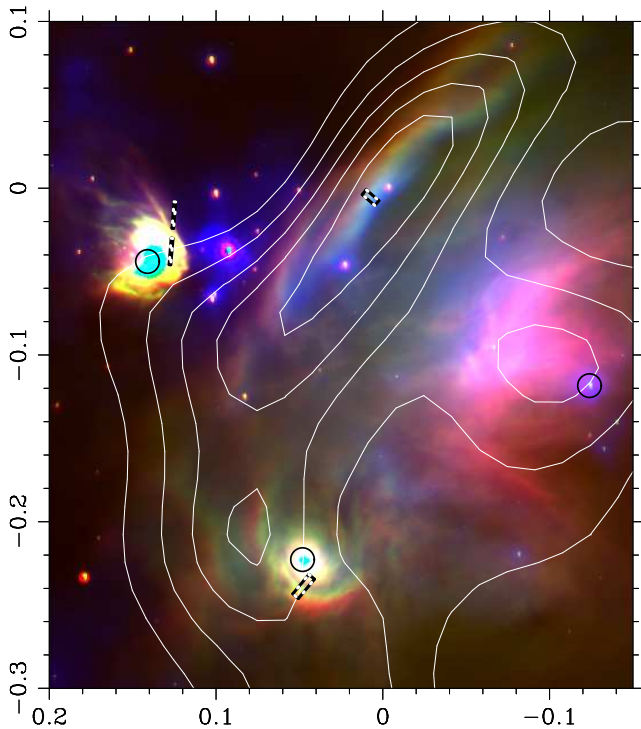


Figure 3. Three-colour image of ρ Oph W: **red**: MIPS $24\mu\text{m}$ **green**: IRAC 4 at $8\mu\text{m}$, dominated by the $7.7\mu\text{m}$ PAH band **blue**: 2MASS K_s -band image. x - and y -axis show offset RA and DEC from ρ Oph W, in degrees. The dashed black and white boxes indicate the extraction apertures for the *Spitzer* IRS spectroscopy discussed in Sec. 5.3 (the apertures near S 1 are narrower than the drawing line width, hence they appear to be linear and not boxy). The contours follow the 31 GHz emission, as in Fig. 1. The centre of the black circles indicate the positions of the early-type stars S 1, SR 3, and HD147889 (see Fig. 4).

081.C-2003). We used the FEROS echelle spectrograph, at the ESO 2.2 m telescope, which provides full coverage over $3500\text{--}9000\text{ \AA}$ at $R = 50000$. We also found two spectra from Feb. 2006 in the ESO archive (programme 076.C-0164).

3.3.2 UNSW-MOPS

The UNSW-MOPS³ spectrometer on the Mopra telescope, a 22 m single-dish, allows the acquisition of area-spectroscopy data cubes up to $\sim 0.6\text{ km s}^{-1}$ in spectral resolution and with a bandwidth of $\sim 2 \cdot 10^3\text{ km s}^{-1}$ (in zoom mode).

Radio recombination lines (RRLs) are diagnostics of physical conditions. In particular low-frequency carbon RRLs have been reported from ρ Oph and other PDRs in reflection nebulae (Pankonin & Walmsley 1978). We attempted to detect the high-frequency carbon RRL system of ρ Oph W using UNSW-MOPS. We acquired 20×20 arcmin on-the-fly scans centred on ρ Oph W and the following rest-frame frequencies (in GHz): in the K band, C65 α 23.41595, C66 α 22.37532, C67 α 21.39545, C68 α 20.47197, C69 α 19.60089, C70 α 18.77853, C71 α 18.00153, C72 α 17.26682, C73 α 16.57156, and in the W band, C42 α 85.73114 and C43 α 79.95252. All 9 K-band frequencies could be mapped simultaneously in zoom mode, for a total of 40 mn. The W-band map represented 2 h.

Data reduction was carried out with the “livedata” and “gridzilla” packages. We chose to resample the data cubes into 5 arcmin square pixels. The 1σ noise was 0.366 MJy sr^{-1} (or 43 mK) for C73 α , and 188 MJy sr^{-1} (or 832mK) for C42 α . No lines were detected.

3.4 Additional archive data

The *WMAP* satellite (Hinshaw et al. 2007) provides low-resolution images of ρ Oph in 5 bands at 23, 33, 41, 61,

³ <http://www.narrabri.atnf.csiro.au/mopra/mops/>

and 94 GHz, with average beam-widths of 0.88, 0.66, 0.51, 0.35, and 0.22 deg, respectively. Despite their low resolution, the *WMAP* data allow the extraction of the radio spectral energy distribution (SED).

3.5 Additional archive data

The Parkes-MIT-NRAO survey at 5 GHz traces H I free-free emission from H II regions (hereafter PMN survey, Condon et al. 1993, as presented in *SkyView*, <http://skyview.gsfc.nasa.gov>). The PMN survey at 5 GHz is strongly affected by flux loss, or missing low spatial frequency due to high-pass filtering. The ρ Oph W region includes extended negatives, indicative of survey artifacts. We estimated the level of filtering artifacts in PMN by comparing with diffuse H II regions (selected from Lockman et al. 1996, hereafter LPH96) in the Effelsberg 2.7 GHz survey (Reich et al. 1990). We extract flux densities as in ρ Oph W (i.e. using a circular aperture 45 arcmin indiameter), and scale with a free-free index. The flux density recovered by PMN is 87% in the case of relatively compact RCW 6 (~ 6 arcmin), 25% in LPH96 201.663+1.643 (~ 15 arcmin, see also the analysis in Dickinson et al. 2006), and only 6% in LPH96 78.229+3.716 (a filament ~ 1 deg long and ~ 15 arcmin wide). It appears that the flux recovered by PMN in the case of ρ Oph W could be as low as 5–10 %.

Another probe of the diffuse emission in ρ Oph is the 2MASS survey <http://www.ipac.caltech.edu/2mass/>. The 2MASS- K_s image produced by the Montage⁴ mosaicing software, shown in Fig. 3 and 5, is an interesting comparison point with the CBI image (see Sec. 4.1 and Sec. 8.4.2).

Our analysis also makes use of the Southern H-Alpha Sky Survey Atlas (SHASSA Gaustad et al. 2001). Another map useful in constraining the radio properties of ρ Oph is that of Baart et al. (1980), who report a 2.3 GHz map of the ρ Oph region, with a beam of 20 arcmin FWHM.

4 OBSERVED PROPERTIES

4.1 Morphology

The most conspicuous feature in the CBI MEM model, also shown in Fig. 4 b, is the ρ Oph W PDR, at the origin of coordinates. The *WMAP* 33 GHz contours in Fig. 4b confirm the bulk morphology of the CBI image.

We indicate in Fig. 4a the positions of the early-type stars S 1 (Grasdalen et al. 1973), SR 3 (Elias 1978, EM* SR 3 in SIMBAD, also known as Elia 2-16), and HD147889. These three stars, undetected in the CBI maps, excite the region and serve as reference points.

Inspection of Fig. 4c leads to the conclusion that the 31 GHz emission from ρ Oph is not the Rayleigh-Jeans tail of the sub-mm-emitting large dust grains (“standard dust” hereafter). If the 31 GHz emission was due to standard dust, it should follow 94 GHz and 178 μ m. Both ISO 178 μ m (in red in Fig. 4c) and *WMAP* 94 GHz trace standard dust. But the CBI contours are offset to the North-West. The peak in *WMAP* 94 GHz is separated by 14 arcmin from the peak in the CBI model. The 94 GHz dust has been resolved into

a system of cold dust clumps by sub-mm bolometer arrays (e.g., Young et al. 2006; Ridge et al. 2006).

The PMN image in Fig. 4a shows two features: extended emission about HD147889, which having an H α counterpart is a faint H II region, and the point source LFAM 21 (J162700.0-242640*, ~ 60 mJy at 5GHz, Gagné et al. 2004), undetected at higher frequencies. Also shown in Fig. 4a are contours at 10 and 20 of the visual extinction map A_V from Ridge et al. (2006)⁵. A_V traces the total column density of material, i.e. the total mass density of the cloud.

Diffuse mid-IR emission ($< 60 \mu$ m) from ρ Oph is interpreted as stochastic heating of VSGs (Bernard et al. 1993). In the dust model of Draine & Li (2007) VSGs are regarded as large polycyclic aromatic hydrocarbons (PAHs). Only the smallest VSGs, or PAHs, can reach spinning frequencies of ~ 30 GHz. Thus for spinning dust a close correspondence is expected between the CBI and mid-IR templates. There are indeed similarities between 31 GHz and *ISO* 46 μ m (in blue in Fig. 4c): both are found near HD147889, while the far-IR emission is located about S 1 and to the south-east.

But there are important differences between the CBI image and the IR templates. In Fig. 3 we compare near- and mid-IR maps with the CBI contours. IRAC and MIPS aboard *Spitzer* provided high resolution mosaics of ρ Oph at near- and far-IR wavelengths. The dust-heating flux from S 1 produces the most conspicuous mid- and far-IR nebula in the entire ρ Oph region (e.g. the PAH 6.7 μ m band image in Abergel et al. 1996). Yet neither S 1 nor SR 3 have 31 GHz counterparts. It can also be noted that the photospheric IR emission is absent in the CBI maps (as is the case in LDN 1622, Casassus et al. 2006).

The IR emission shifts to longer wavelengths radially away from HD147789: at increasing wavelengths the emission from ρ Oph W moves to the N-E. It is surprising that the best match to the CBI contours of ρ Oph W turns out to be the 2.2 μ m diffuse emission in the 2MASS K_s -band, shown in blue in Fig. 3, and in grey scale in Fig. 5. The pointing uncertainty of the CBI is < 0.5 arcmin (e.g. Casassus et al. 2006) - the phase calibrator J1626-298 was offset by only 0.2 arcmin from the phase centre. Thus the CBI data are sensitive to the ~ 2 arcmin translation in ρ Oph W, when seen in MIPS 24 μ m and 2MASS K_s -band.

The only 2MASS counterpart to the CBI contours are the emission peaks along ρ Oph W. The north-south extension of the CBI contours to the east of SR 3 is undetectable in 2MASS, but we note that this region has higher extinction than ρ Oph W (see Sec. 5.1).

Another conspicuous feature of the 2MASS image is the nebulosity about HD147889, which is probably the near-IR counterpart to the diffuse H II region seen in PMN. An extended 2MASS source at J162622-242301, at $(\Delta\alpha, \Delta\beta) \approx (+0.09, -0.04)$ and between S 1 and W, corresponds to the disk-like envelope surrounding the young stellar object GSS 30 IRS 1 (Chrysostomou et al. 1996).

4.2 Spectrum

In Fig. 6 we have constructed the spectral energy distribution of ρ Oph A using the flux densities given in Table 1. The

⁴ <http://montage.ipac.caltech.edu/>

⁵ <http://www.cfa.harvard.edu/COMPLETE>

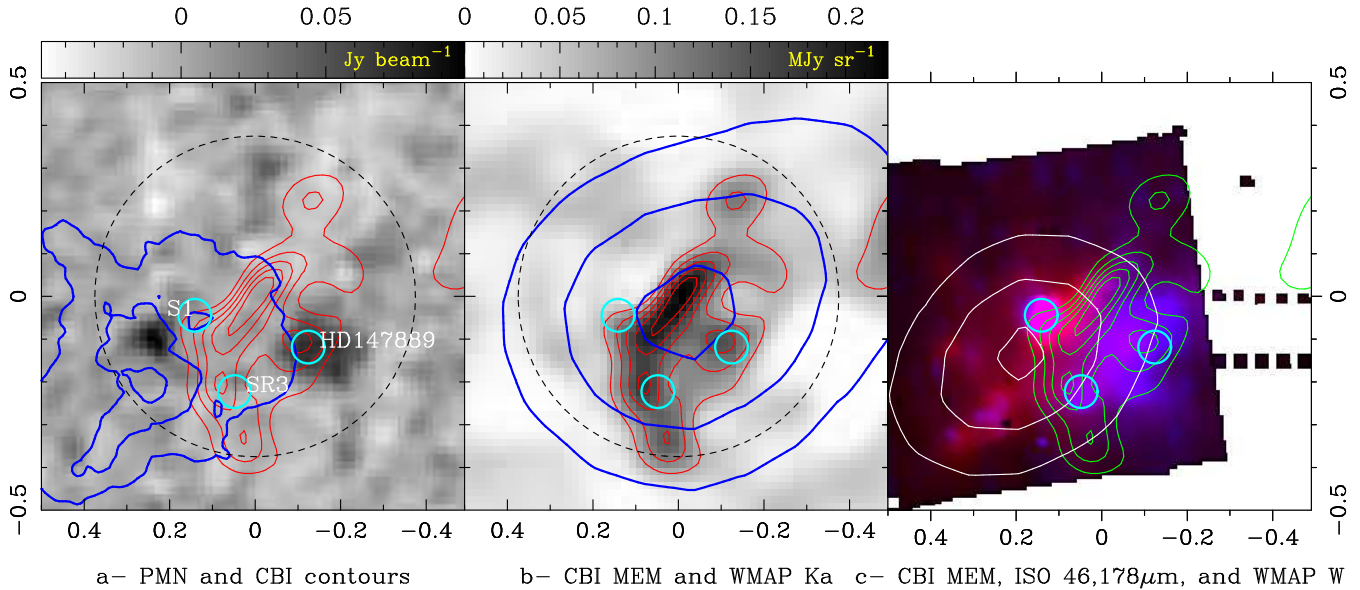


Figure 4. Morphological evidence ruling out standard dust or optically thin H I free-free as the origin of the 31 GHz emission. x - and y -axis show offset RA and DEC from ρ Oph W, in degrees. The centre of the cyan circles indicate the positions of the early-type stars S 1, SR 3, and HD147889. **a-** CBI MEM contours overlaid on the PMN image (4.85 GHz), with A_V in blue contours at 10 and 20. **b-** The CBI MEM image is shown in grey scale in MJy sr $^{-1}$, with the same contour levels as in Fig. 1. *WMAP* 33 GHz is shown in blue contours at 2.52, 2.99, and 3.37 K. **c-** CBI MEM contours overlaid on an *ISO* colour map with 46 μ m in blue and 178 μ m in red. *WMAP* 94 GHz is shown in white contours at 1.21, 1.51, and 1.75 K.

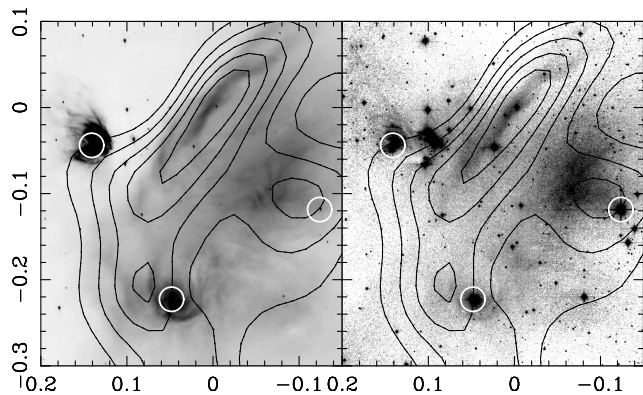


Figure 5. The 2MASS-CBI correlation. The image is an overlay of the CBI MEM contours on the IRAC 8 μ m (left) and 2MASS K_s -band images (right). x - and y -axis show offset RA and DEC from ρ Oph W, in degrees. It may be appreciated that the 2MASS and IRAC 8 μ m emissions correlate with 31 GHz in ρ Oph W.

WMAP flux densities are extracted from a circular aperture equal to the CBI primary beam, without background correction.

It is difficult to extract spectral index information from the 10 CBI channels because the u, v coverage varies with frequency: flux loss, or the fraction of the flux density in the CBI 45 arcmin aperture that is filterout out, varies with both channel frequency and sky image. A template close in morphology to the 31 GHz emission could have been used to extract accurate channel by channel flux densities. But no such template is available. The cross-correlation between the CBI data and simulated visibilities on the prior image

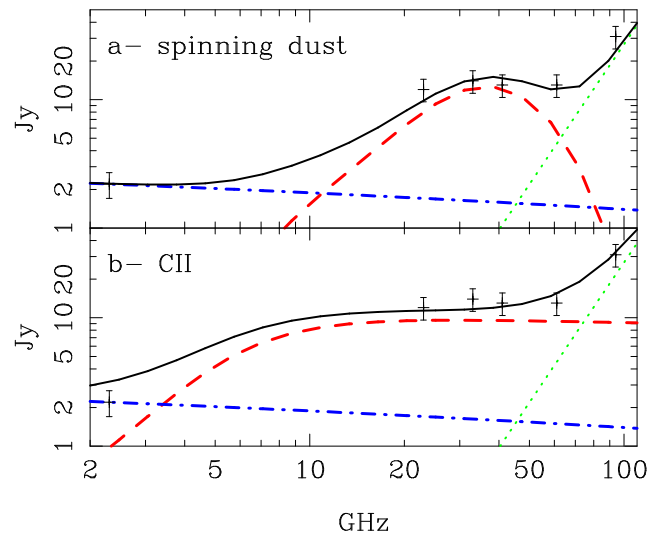


Figure 6. The cm-wave spectrum in a 45.5 arcmin circular aperture centred on ρ Oph W. All data points are extracted from the *WMAP* images, except for the 2.3 GHz point, which is taken from Baart et al. (1980, see Sec. 4.4). The solid black line is a fit to the data that includes a modified blackbody, in green dotted line (with $T_d = 23$ K and $\beta = 1.7$), a diffuse free-free component, shown as a dash-dotted blue line, and in red-dashed line either a spinning dust component (**a- spinning dust**, for the ‘DC’ environment), or a cold C I thermal component stemming from an ensemble of PDR sheets seen edge-on (**b- C II**).

shown in Fig. A2e gave high reduced χ^2 values (~ 2.4) and r correlation coefficients of ~ 0.6 . The MEM model itself

Table 1. Observed flux densities inside the half-maximum contour of the CBI primary beam. Root-mean-square uncertainties are of order 20%.

ν^a	2.3 ^c	23 ^d	31 ^e	33 ^d	41 ^d	61 ^d	94 ^d
$F(\nu)^b$	2.2	12	7.9	14	13	13	31

^a Frequency in GHz. ^b Flux density in Jy, with uncertainties of 20%. ^c From Baart et al. (1980). ^d From *WMAP* ^e CBI flux density before correcting for flux loss.

cannot be used as a template in this case because it is limited in resolution by the dynamic range of the data.

The sub-mm continuum in ρ Oph A can be estimated from the *WMAP* 94 GHz and far-IR points, as a single modified black body with an emissivity index β . For this purpose we used the IRIS (Miville-Deschenes & Lagache 2005) re-processing of the *IRAS* survey (Wheelock et al. 1991), and extracted flux densities in a circular aperture equal to the CBI primary beam (the *ISO* images lack coverage in the Eastern side of the photometric aperture). The observation of a sub-mm flux density is required to constrain the value of β . We did not use the SCUBA maps of ρ Oph because they are strongly filtered. We estimated by comparison with the expected sub-mm continuum that the diffuse emission that is filtered out of the bolometer data in a 45 arcmin aperture can amount to $\sim 85\%$.

4.3 CBI flux loss

The CBI image is not sensitive to the lowest spatial frequencies; uncertainties in the comparison data are approximate and stem mostly from mismatched angular scales, not thermal noise. In particular the *WMAP* beam at 33 GHz is approximately Gaussian with FWHM ~ 49 arcmin (Bennett 2003), so that the emission within the CBI beam is somewhat convolved with the surroundings. In turn, part of the flux at low spatial frequencies is filtered out in the interferometer data.

We have simulated CBI observations on two templates: IRAC $8\mu\text{m}$, after removing stars by median-filtering, and IRIS 1, a $12\mu\text{m}$ template (Miville-Deschenes & Lagache 2005). After reconstruction with a blank prior (as in Sec. A), we find that 41.3% of the IRAC $8\mu\text{m}$ flux within the CBI primary beam is recovered by the simulation; and 51.4% in the case of IRIS 1. The same algorithm applied to the CBI visibility produces the image shown on Fig. A2d, and a flux density of 5.0 Jy, which when compared to 14 Jy in *WMAP* 33 GHz implies that the fraction of flux density recovered in the blank-prior reconstructions is 35%. But the image prior used in our best CBI reconstructions allow recovering part of the extended emission. Comparison of the flux density obtained from the restored image on Fig. A2a and with *WMAP* 33 GHz shows that, with the use of a prior, 56% of the signal is recovered by the CBI.

4.4 HI free-free

The *WMAP* 33 GHz and SHASSA images shown in Fig. 7 illustrate that ρ Oph W is superposed on an extended background, which is probably the free-free counterpart to the

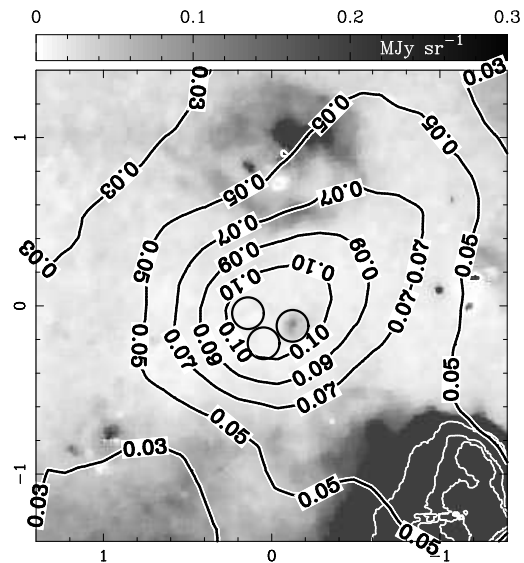


Figure 7. $H\alpha$ and HI continuum towards ρ Oph. The Fig. shows an $H\alpha + [N II]$ image of the ρ Oph region, as extracted from SHASSA, and scaled to the corresponding $T_e = 8000$ K free-free continuum at 33 GHz, in MJy sr^{-1} , without correction for reddening. The black and white contours follow *WMAP* 33 GHz, also in MJy sr^{-1} . The SHASSA emission from Gum 65 to the south-west is traced in white contours at 1.0, 5.0, and 10 MJy sr^{-1} . The circles indicate the positions of S 1, SR 3, and HD147789. x - and y -axis show offset RA and DEC from ρ Oph W, in degrees.

$H\alpha$ emission. There are however intriguing features in Fig. 7: the bright $H\alpha$ source to the south-west (a bright H II region surrounding σ Sco, known as Gum 65 or S 9) should correspond to 33 GHz free-free levels at least a factor of ten higher than seen in *WMAP* Ka. We believe this is due in part to dilution in the *WMAP* beam, but also to [N II] doublet contamination in the SHASSA filter, which can be of order 50% in photoionised nebulae (e.g. in the Helix, see Sec. 2.3 in Casassus et al. 2004), or even higher in shocks. Nitrogen is found singly ionised in the outer bounds of ionisation-bounded nebulae, which are the surface regions sampled by the (extinction sensitive) SHASSA filter.

In the 2.3 GHz map of Baart et al. (1980) the CBI primary beam lies in a region of uniform emission, with a brightness temperature of ~ 100 mK. The integrated flux density inside our photometric aperture is thus ~ 2.2 Jy at 2.3 GHz, or ~ 1.7 Jy at 31 GHz⁶.

The PMN flux density in the 45 arcmin photometric aperture is essentially zero. Yet the SHASSA survey shows substantial diffuse $H\alpha$ in the region of ρ Oph W. The total $H\alpha$ flux in the CBI primary beam, if due to the diffuse 8000 K plasma discussed by Dickinson et al. (2003), implies that the free-free level at 5 GHz should be at least ~ 2.5 Jy. After correction for the average value of extinction inside the CBI beam but outside the dark cloud itself,

⁶ Given that the CBI flux density measured from the blank-prior CBI image in Fig. fig:CBI is 5.0 Jy while *WMAP* 33GHz sees 14 Jy, of which 1.7 Jy are diffuse free-free, we obtain that the CBI recovers 40% of the non-free-free emission (consistent with Sec. 4.3, see also Sec. 8.5)

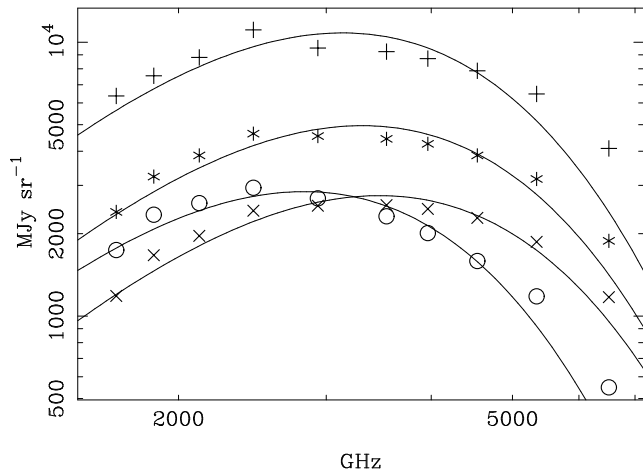


Figure 8. Representative ISO LWS specific intensity spectra, at four selected positions in ρ Oph: ρ Oph W (circles), S 1 (pluses), HD 147889 (crosses) and SR 3 (asterisks, scaled by a factor 1.8 for clarity). The solid lines are best-fit grey-body spectra, as discussed in the text and summarised on Fig. 9.

$E(B - V) \approx 1 - 3$ (Schlegel et al. 1998), or $A_V = 3 - 9$ for $R_V = A_V/E(B - V) = 3.1$, the predicted level of free-free emission could reach values of order ~ 10 Jy. Since the 2.3 GHz flux density inferred from Baart et al. (1980) is somewhat less than the minimum allowed by SHASSA, we conclude that the diffuse emission seen by SHASSA is also strongly contaminated by [N II].

5 DUST EMISSION

5.1 IR emission from dust grains

Bulk physical properties of the dust in ρ Oph can be obtained by fitting modified black bodies to the spectra extracted from each spatial pixel of the *ISO* data cube. A single modified black body turns out to give a fairly good fit, despite expected temperature gradients, especially from stochastic heating of the smaller grains (whose emission, as traced by IRAC 8 μm for instance, is very different from that of the larger grains emitting at 100 μm).

The grey-body parameters are the opacity at 100 μm , τ_{100} , and T_d , the dust temperature. The dust emissivity index is determined by its anticorrelation with dust temperature, as reported by Dupac et al. (2003): $\beta = 1/(0.4 + 0.008T_d)$. τ_{100} is related to N_H , the H-nucleus column density, by $N_H = 4 \cdot 10^{24} (\lambda/100 \mu\text{m})^\beta \tau_{100} \text{ cm}^{-2}$ (Draine & Lazarian 1999b). Example infrared spectra are shown on Fig. 8.

The resulting temperatures, column densities and dust emissivities are shown in Figures 9a, 9b and 9c. The maximum value of N_H in Fig. 9b is $2.3 \cdot 10^{23} \text{ cm}^{-2}$, and the temperature varies over 20–40 K. The early type stars S 1, SR 3 (see Sec. 8.1) are coincident with temperature peaks, as expected from grains in radiative equilibrium with the stellar UV radiation. But neither S 1 nor SR 3 correspond to peaks in column density. N_H peaks close to S 1, but its morphology follows that of the ρ Oph A molecular core.

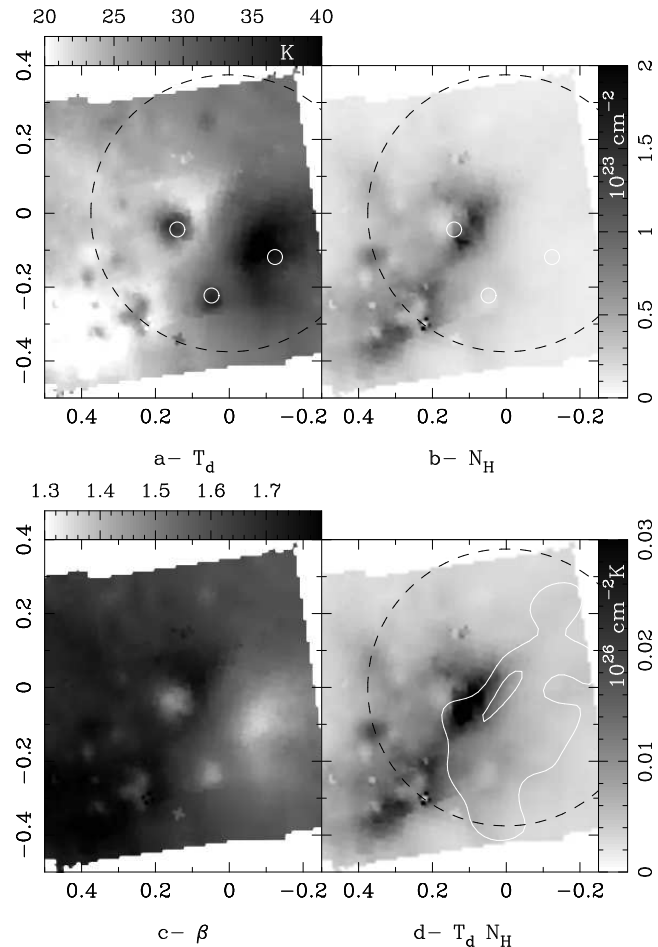


Figure 9. Axes labels and symbols follow from Fig. 4. **a-** Dust temperature in gray scale, the CBI primary beam and the positions of S 1, SR 3 and HD147789 are indicated. **b-** The H-nucleus column density inferred from the far-IR *ISO* data. **c-** Dust emissivity (or temperature spectral index) inferred from the β - T_d anticorrelation of Dupac et al. (2003). **d-** Gray scale image of the product of the H-nucleus column density N_H times the dust temperature T_d , in units of $10^{26} \text{ m}^{-2} \text{ K}$. Also shown are the lowest and highest contours of the CBI MEM models, at 0.067 and 0.197 MJy sr^{-1} .

Therefore the IR circumstellar nebulae about S 1 and SR 3 are radiation-bounded rather than matter-bounded.

The total mass in the *ISO* field, $M_T = m_p D^2 \int d\Omega N_H$, is $922 M_\odot$. Considering the numerous assumptions implicit in converting dust emissivities to H-nucleus densities, this mass estimate is consistently close to $\sim 2500 M_\odot$ given by Liseau et al. (1995, 1999). But the mass seen by *ISO* is much less than the $7400 M_\odot$ derived from the near-IR extinction (Ridge et al. 2006). Perhaps the extinction has been overestimated, or there are very cold regions in ρ Oph not sampled by *ISO*.

We also obtain a mass of $65 M_\odot$ for ρ Oph W, if its extension is defined by a 31 GHz intensity threshold of $0.124 \text{ MJy sr}^{-1}$ in the MEM model (see Fig. 1). The mass above a 31 GHz intensity threshold of $10^{-3} \text{ MJy sr}^{-1}$ is $359 M_\odot$.

5.2 Magnetic dust

The magnetic dipole emission from magnetic fluctuations in ferromagnetic grains results in a cm-wave enhancement of the grain emissivity (Draine & Lazarian 1999). At cm-wavelengths classical (not VSG) dust is in the Rayleigh-Jeans regime, so that magnetic dust emission should be proportional to the product of the column of ferromagnetic grains and their temperature. Under the assumption that ferromagnetic grains, if they exist, are uniformly mixed with the rest of the dust, the CBI image should be proportional to the product of the dust column N_d and temperature T_d for constant dust-to-gas ratio ($N_d \propto N_H$).

It can be seen in Fig. 9d that the morphology of the CBI MEM contours is very different from that of the product $N_H T_d$, which instead follows the far-IR emission. Since we cannot find any reason why ferromagnetic grains, if they exist, would be found preferentially in ρ Oph W, we conclude that magnetic dust is inconsistent with the *ISO* data.

Another difficulty for magnetic dust is the lack of detectable polarization. Draine & Lazarian (1999, their Fig. 9) predict polarization fractions f from perfectly aligned ferromagnetic grains. For their hypothetical material 'X4' the predicted fraction at 31 GHz is at least $f = 25\%$. X4 is the only material considered by Draine & Lazarian (1999) whose emissivities reach the levels required by the anomalous foreground. Martin (2007, his Table 2) quantifies the degree of grain alignment through a reduction factor R , which ranges from 0.19 to 0.67 for a wide variety of grain geometries. Thus the polarization expected from magnetic dust is at least 4.7%. However, the CBI data place a strict 3σ polarization upper limits of 4.8% in the specific intensity at the peak in ρ Oph W - and only 1% in the 45 arcmin photometric aperture.

5.3 Spinning dust

The spinning dust emissivities, being linear proportional to the density n_H (as dust emissivities in general), could be more important in diffuse media relative to emission mechanisms based on binary encounters, which are quadratic in n_H . With its very steep low frequency spectral index, $\alpha \sim +3$, spinning dust explains the lack of low-frequency emission.

Spinning dust gives a remarkably good fit to the ρ Oph W SED (see Fig. 6) if $\beta = 1.7$, which is within the range of observed values (Dupac et al. 2003). Higher emissivities result in a drop at ~ 60 – 90 GHz, which misses the WMAP 94 GHz data point. The best fit spinning dust spectrum is obtained for the 'DC' case of Draine & Lazarian (1998b). Spinning dust requires that the product $n_H f \sim 10^5 \text{ cm}^{-3}$, where f is the volume filling factor.

No local 31 GHz peaks are observed at the positions of S 1 and SR 3. Although part of the emission surrounding S 1 and SR 3 could be scattered light in IR reflection nebulae, the *Spitzer* IRS area-spectroscopy highlights very bright PAH bands in the circumstellar nebulae around S 1, SR 3 and ρ Oph W. The absence of S 1 and SR 3 in the CBI data may be inconsistent with spinning dust, since the proximity of early type stars should result in high spinning dust emissivities, provided VSGs are not depleted. The environment around S 1 corresponds to the 'RN' case of

Draine & Lazarian (1998b): the Castelli (2003) model atmospheres give a UV flux parameter $\chi \approx 5000$ (as defined in Draine & Bertoldi 1996). In this case the predicted spinning dust emissivity per unit H-nucleus column density is $10^{-17} \text{ Jy sr}^{-1} \text{ cm}^2$ at 31 GHz. The observed column densities towards S 1 is 10^{23} cm^{-2} (see Sec. 5.1), so the emergent 31 GHz intensity from S 1 should be 1 MJy sr^{-1} , which is a factor of 10 larger than the observed peak 31 GHz intensities (which are found in ρ Oph W and not toward S 1), and a factor of 40 larger than a strict upper limit of $25 \cdot 10^{-3} \text{ MJy sr}^{-1}$ in S 1 (see Table 2).

We can take into account the possibility of VSG depletion by examining the ratios of PAH and 31 GHz intensities. The dust-heating radiation field can be parametrised, as in Draine & Li (2007), by scaling the interstellar radiation field in the solar neighbourhood (Mathis et al. 1983). The dimensionless parameter U measures the average intensity of radiation in $4\pi \text{ sr}$, integrated from 0.09 to $8 \mu\text{m}$. The spinning dust emissivity per nucleon is remarkably independent of the intensity of UV radiation (Draine & Lazarian 1998b, their Fig. 9), while the flux in the PAH bands is linear in U (for instance see Fig. 13 in Draine & Li 2007). Therefore, if PAHs are involved in the 31 GHz emission, the intensity ratio $R = I_\nu(31\text{GHz})/I_{\text{PAH}}(11.3 \mu\text{m})$ should be inversely proportional to U . R is independent of the PAH abundance since it enters linearly both in $I_\nu(31\text{GHz})$ and I_{PAH} . Given that the spinning dust emissivities per nucleon (Draine & Lazarian 1998b) vary by at most a factor of 10 for environments with extremely different physical conditions, we can conservatively assume that $R \times U$ should not vary by more than a factor of 10 when comparing widely different regions.

The IRS data allow extracting fluxes for the PAH band at $11.3 \mu\text{m}$, $F_{\text{PAH}}(11.3 \mu\text{m})$, in two rectangular apertures near S 1, one near SR 3, and one in ρ Oph W, indicated as black and dotted-white boxes on Fig. 3. We subtracted a linear continuum under the $11.3 \mu\text{m}$ band, as well as a sky background PAH $11.3 \mu\text{m}$ intensity of $2 \cdot 10^{-7} \text{ W m}^{-2} \text{ sr}^{-1}$, obtained by scaling the observed PAH intensities following the IRAC $8 \mu\text{m}$ image. The background PAH intensity is only 5 times fainter than observed in the S1 off aperture ($9.98 \cdot 10^{-6} \text{ W m}^{-2} \text{ sr}^{-1}$ before background correction).

Until we obtain higher-resolution data our estimates of the 31 GHz specific intensities $I_{31 \text{ GHz}}$ are dependent on the MEM model. In the brightest regions, as in ρ Oph W, we assume 10% uncertainties. The product of the IRS extraction solid angle times the CBI intensity at the centroid of the ρ Oph W aperture is an approximation to $F_\nu(31 \text{ GHz})$, the 31 GHz flux density. For the fainter regions we use the prior that the emission is due to spinning dust (which is the aim of this test): The circumstellar nebulae around S 1 and SR 3 are ~ 3 arcmin in diameter and so should appear as point sources in the CBI maps. A formal fit to the MEM visibility residuals for point sources at the locations of S 1 and SR 3 gives 31 GHz flux densities of $1.3_{-4}^{+7} \text{ mJy}$ and $2.0_{-3}^{+7} \text{ mJy}$, respectively, which can be converted into intensities assuming uniform nebulae. For S 1off we scale the 31 GHz intensity in the S 1 aperture by the product of PAH $11.3 \mu\text{m}$ intensities times U (i.e. as the inverse squared projected distance).

The unattenuated intensity of dust-heating radiation, parametrised by U , can be evaluated at the projected distance from the exciting stars to the centre of each IRS aper-

Table 2. Observations derived from the CBI and PAH 11.3 μm intensities in the *Spitzer* IRS apertures.

	$R \times U^{a,b}$	U^c	$I_{31\text{GHz}}^d$	I_{PAH}^e	d^f
ρ Oph W	27.5 ± 2.7	66	$2.2 \pm 0.2(-1)$	$3.3(-6)$	10.4
SR 3	$<1.2 \pm 3.2$	<238	$3.2 \pm 8.4(-3)$	$3.8(-6)$	0.97
S1	1.0 ± 4.9	1076	$1.7 \pm 8.4(-3)$	$1.1(-5)$	0.92
S1 off	$<1.0 \pm 1.1$	246	$5.2 \pm 5.9(-4)$	$8.0(-7)$	1.92

^a $R = I_\nu(31\text{GHz})/I_{\text{PAH}}(11.3 \mu\text{m})$ ^b Normalized to the value in the S 1 off aperture. ^c Unattenuated UV field parameter. ^d CBI MEM specific intensities in MJy sr^{-1} . ^e PAH 11.3 μm intensity in $\text{W m}^{-2} \text{sr}^{-1}$. ^f Projected distance from exciting star, in arcmin. ^g parenthesis indicate a power of ten exponent multiplying both the average values and their uncertainties.

ture, using the model atmospheres of Castelli (2003)⁷ and the stellar parameters given in Sec. 8.1. We obtain the properties listed in Table 2. Taking into account the uncertainties, the product $R \times U$ is consistent with variations by less than a factor of 10. A marginal exception may be the comparison between S 1off and ρ Oph W, where the 31 GHz uncertainties are reduced relative to S 1 because of the hypothesis that the 31 GHz intensity in S 1off scales with $U \times I_{\text{PAH}}$ relative to S 1. In the S 1off - ρ Oph W comparison, taking 3 σ shifts in $R \times U$ can bring its variations down to a factor of 4, and so in agreement with spinning dust.

A source of uncertainty is the correction for UV attenuation, which may affect all lines of sight in Table 2. Attenuation is most important for S1 off, since the circumstellar nebula around S 1 is probably ionisation-bounded (see Sec. 5.1). The value in Table 2 is therefore an upper limit. Similarly for SR 3, which is obscured in the visible. On the other hand S 1 is bright in the visible, so its circumstellar nebula stems from the walls of a wind-blown cavity driven by S 1 into the ρ Oph A core. Thus UV attenuation should be negligible in the S 1 IRS aperture. According to the model of Liseau et al. (1999), HD 147889 is separated from LDN 1688, so that its UV luminosity should be fairly unattenuated towards ρ Oph W.

Could physical conditions in S 1 and SR 3 be such that spinning dust is quenched by mechanisms not contemplated by Draine & Lazarian (1998b)? The possibility of vanishing grain polarization can be discarded. According to the PAH ionisation diagnostic of Draine & Li (2001, their Fig. 16), the PAH band fluxes given by Boulanger et al. (1996), extracted from an aperture 10 arcmin north of ρ Oph W, correspond to neutral PAHs. Any photoelectric charge expected in the intense UV-fields of S 1 and SR 3 increases quadratically the spinning dust emissivity (Eq. 11 in Draine & Lazarian 1998b). But it could be that the radiation field from HD 147889 is sufficiently hard to boost the spinning dust emissivity through VSG-ionisation, and yet not completely deplete the grains. We used the IRS spectra to place S 1 in the PAH-colour diagram of Draine & Li (2001, their Fig. 16), finding it lies close to ρ Oph W - i.e. at the locus of neutral PAHs. Another interesting possibility is that perhaps PAH rotation brakes to lower frequencies in the vicinity of SR 3 and S 1, maybe as a consequence of grain alignment in in-

tense magnetic fields (which are not considered in Draine & Lazarian 1998b).

Yet another alternative to explain the lack of 31 GHz emission from S 1 and SR 3 is that the spinning VSGs are not related to PAHs, so that they do not emit in the PAH bands. For instance they could perhaps be nano-silicates (e.g. Witt et al. 1998) very fragile to UV radiation, or maybe chain-like carbonaceous molecules. If so the existing spinning dust models must be revised, since they are calculated for aromatic carbonaceous grains, including a population of sheet-like grains (i.e. PAHs).

Iglesias-Groth (2006, 2005) has proposed hydrogenated fullerenes as a carrier for the 31 GHz emission. Perhaps the polarized fullerenes could be depleted near S 1 and SR 3. But at present we lack diagnostics of such fullerenes to test this alternative. As proposed by Webster (1992) fullerenes could also be the carriers of the diffuse interstellar bands (DIBs). Spectroscopy of stars in the background of ρ Oph is required to examine the possibility of a link between the DIBs and the anomalous foreground.

6 CI CONTINUUM

6.1 Cold plasmas in PDRs

The outer layers of molecular clouds are composed of atomic hydrogen. The ionisation energy of H_2 is 15.4 eV, while the H_2 dissociation continuum starts at 14.7 eV, both of which are attenuated by H I ionisation. In practice H_2 photodissociation occurs in the radiative cascade following bound-bound absorption of photons with discrete energies in the range 11.3 – 13.6 eV (e.g. Tielens 2005). Thus the bulk of the ρ Oph cloud is largely neutral.

All photons harder than 13.6 eV are absorbed in the vicinity of HD147889, producing a ~ 5 arcmin diffuse H II region (about 0.2 pc in physical size). Yet a residual charge density exists in the neutral layers of ρ Oph exposed to radiation from HD147889. C-ionising photons with energies in a continuum between 11.3 eV and 13.6 eV penetrate deep inside the exposed neutral layers of ρ Oph W. C-ionisation extends into molecular layers. Other metals with ionisation potentials inferior to 13.6 eV, most notably sulfur, also contribute to the ionisation fraction $x = n_e/n_{\text{H}}$, but in proportion to their abundance.

Another source of ionisation in molecular clouds is the cosmic-ray ionisation of H_2 . For an isolated molecular cloud subjected to the average interstellar cosmic ray ionization rate ζ , molecular line observations have yielded $x \approx 10^{-8}$. Specifically for ρ Oph Wootten et al. (1979) give $x = 2.6 \cdot 10^{-7}$. However the molecular line diagnostics in Wootten et al. (1978) trace the dense core in ρ Oph A, and may not be representative of ρ Oph W. Is it possible that in ρ Oph W the vicinity of HD147889 increases ζ sufficiently so that H_2^+ also contributes to x ? Probably not, since the ratio of projected distances between ρ Oph A and ρ Oph W to HD147889 is ~ 2 , which would only raise ζ by a factor of 4, and yield an x value still 2 orders of magnitude below the

⁷ as given in <http://wwwuser.oat.ts.astro.it/castelli/grids.html> carbon abundance.

6.2 C I model

Here we estimate the expected intensity levels of free-free emission due to C^+ encounters with free electrons (C I continuum) from the cold plasma in ρ Oph W. Although the ionisation fraction in PDRs is very small, $x \sim 10^{-4}$, the free-free emissivity is $\propto 1/\sqrt{T_e}$ and biased towards lower temperatures. A temperature of ~ 50 K is representative of most of the emissivity-weighted C II region in the models of Liseau et al. (1999) and Habart et al. (2003). A shortcoming of the present model is that it requires a clumpy medium with very high H-nucleus densities, of order 10^7 cm^{-3} , and small volume filling factors, $f \sim 10^{-4}$.

The available data lead us to consider an ensemble of dense neutral clumps, with an ionisation fraction $x \sim 10^{-4}$ (the abundance of C), a total extent $\theta_N \approx 20$ arcmin, and covering a solid angle $\Omega_N \approx \pi(\theta_N/2)^2$. Since ρ Oph W is undetected in the HRAO data of Baart et al. (1980), with a 20 arcmin beam and a rms sensitivity of 30 mK, at 2.3 GHz the total emission from the clumps should be less than $F_c(2.3 \text{ GHz}) \approx \Omega_N \times 3I_{\text{rms}}(2.3 \text{ GHz}) \approx 2 \text{ Jy}$. The total flux density seen by *WMAP* at 33 GHz and not attributed to H I free-free is 12.3 Jy. Thus the clumps must be optically thick at 2.3 GHz, and cover a solid angle inferior to $\Omega_c \approx F_c(2.3 \text{ GHz})/B_\nu(2.3 \text{ GHz}, T_e = 20 \text{ K}) \approx \pi 1.5^2 \text{ arcmin}^2$, where B_ν is the Planck function. Additionally, the clumps, while still optically thick at 5 GHz, are not detected in PMN, with a beam $\theta_{\text{PMN}} = 3.7$ arcmin FWHM and an rms noise of $I_{\text{PMN}} \sim 100 \text{ mJy beam}^{-1} = 0.67 \text{ MJy sr}^{-18}$. Therefore an individual clump must be beam-diluted in PMN and cover a solid angle less than $(I_{\text{PMN}}/B_\nu(5 \text{ GHz}, 20 \text{ K}))(\pi/(4 \ln 2))\theta_{\text{PMN}}^2 \approx 3 \text{ arcmin}^2$.

As discussed in Sec. 4.2, the CBI sees about 30–40%⁹ of the total 31 GHz emission. The clump distribution should be sufficiently dense so as to mimick a uniform signal at CBI resolutions, while also extending to θ_N . Thus the inter-clump separation should be (a) less than 8 arcmin, the highest spatial frequency in the CBI *uv*-plane for the configuration used here, and (b) greater or similar to the PMN beam. To make headway, we will assume a number of clumps $N_c = (\theta_N/\theta_{\text{PMN}})^2 \approx 30$.

A plane-parallel geometry seen edge-on gives the highest clump opacities. To maximize the cold free-free opacity given an electron density, each clump would have to be θ_{PMN} in length, equally deep, and only $\Omega_c/(N_c\theta_{\text{PMN}}) \approx 4$ arcsec wide. Higher densities alleviate the need for such large aspect ratios.

What is the density required to explain the 31 GHz flux density with a cold plasma, if we ignore the lower frequency data? In a uniform disk nebula 10 arcmin in diameter, and equally deep, with a C II region temperature of 150 K, we find that electron densities of $n_e = 60 \text{ cm}^{-3}$ reach the observed 31 GHz level. The same result is arrived at by fixing the opacity profile to that of the CBI MEM model. Thus H-nucleus densities of only $n_H \sim 10^5 - 10^6 \text{ cm}^{-3}$ (within

the range observed in ρ Oph W, see Sec. 8.2) account for all of the CBI flux.

6.3 SED fit

The C I continuum model shown in Fig. 6 b consists of a clump ensemble with $N_c = 30$, an electron density of 750 cm^{-3} , and $T_e = 20$ K. Each clump is a narrow sheet only 2 arcsec wide¹⁰, 3.7 arcmin long, and equally deep. The corresponding volume filling factor is $f \sim 10^{-4}$. Uniform disk clumps, with equal depth and diameter and subtending the same solid angle as the sheets, would require electron densities of 2200 cm^{-3} . We favour a sheet-like geometry because of the considerations in Sec. 8.1: The thin sheet geometries could result from limb-brightening of a C II shell centred on HD147889.

The total H-nucleus densities required by the C I model, whatever the geometry of the clumps, are of order $\sim 10^7 \text{ cm}^{-3}$, if all of C is ionised. The corresponding C II region mass is $153 M_\odot$ for sheets, or $45 M_\odot$ for disks, both of which are consistently less than the total mass enclosed by regions with finite $I_{31 \text{ GHz}}$ (see Sec. 5.1).

In order to further test the C I continuum model we searched the ATCA archive for pointings near ρ Oph W. ρ Oph 10 (also known as Doar 21; Encrenaz 1974) was observed in array configuration C397, at frequencies of 1376, 2378, 4800 and 8640 MHz¹¹. The phase centre lies in the 31 GHz ρ Oph W ridge, 2.2 arcmin south of the peak. At 4.9 GHz the ATCA primary beam is 5 arcmin. Yet no clumpy medium is detected with a noise of 5 mJy/beam. Clearly the putative C I clumps, if they exist, should be beam-diluted even inside the 12×7 arcsec² beam: the optically thick flux density in one synthetic beam is 160 mJy, if $T_e = 20$ K. Very thin sheets, ~ 1 arcsec wide, could still fit in.

7 RADIO RECOMBINATION LINES

Radio recombination lines (RRLs) are concomitant to free-free continua. Carbon RRLs have indeed been observed towards ρ Oph, albeit at low resolutions (Brown & Knapp 1974). Here we provide upper limits on the RRL system in ρ Oph W, which require rather cold C II regions ($T_e \sim 20 - 50$ K).

7.1 RRL data from the literature

Pankonin & Walmsley (1978) examined the most complete set of RRL data towards ρ Oph to date. They mapped the neighbourhood of S 1, but did not extend their coverage to ρ Oph W, unfortunately. The highest frequency RRLs considered by Pankonin & Walmsley (1978) are C90 α and C91 α , at ~ 9 GHz, which they interpreted as stemming from circumstellar gas about S 1, with electron densities $n_e \sim 15 \text{ cm}^{-3}$ and $T_e \sim 150$ K. This circumstellar C II region was inferred to be less than ~ 2 arcmin in diameter, and

⁸ in which we have taken into account correlated pixels with a factor $\sqrt{N_{\text{beam}}}$, where N_{beam} is the number of pixels that fall in one 3.7 arcmin beam

⁹ this is the ratio of 31 GHz flux densities obtained without the use of a prior to the *WMAP* 33 GHz flux densities

¹⁰ We chose 2 instead of 4 arcsec to better accommodate the 2.3 GHz point

¹¹ ATCA programme C397, PI E. Feigelson

surrounded by a diffuse halo with $n_e \sim 1 \text{ cm}^{-3}$, traced by the lower frequency carbon RRLs. The continuum level expected from such a C II region is $\sim 1 \text{ mJy}$ at 31 GHz, consistent with its absence from the CBI MEM model.

7.2 CBI limits on Ka-band RRLs

The brightest carbon RRLs expected in the 10 CBI channels are C57 α to C62 α . Four 1 GHz wide channels, centred at 27.5, 30.5, 33.5, and 35.5, are free from α RRLs. Yet the CBI flux densities in each channel, inferred by cross-correlation with a processed IRAC 8 μm template, are scattered about a single power law; no decrement is seen in the four channels devoid of RRLs. A 1 σ upper limit to the contribution of RRLs in a single channel is given by the rms dispersion about the best fit power-law, of $\sigma_{\text{RRL}} = 0.04 \text{ Jy}$.

The expected RRL flux in the CBI channels is quite close to the above upper limit. In the C II region model of Sec 6, the flux density from C62 α , at 26.95 GHz, in the 1 GHz wide CBI channel centred on 26.5 GHz, is 0.6 Jy under LTE conditions. However, for $n < 100$ the excited energy levels leading to the emission of α photons are severely depopulated relative to LTE at $\sim 150 \text{ K}$ (Salem & Brocklehurst 1979; Walmsley & Watson 1982)¹². The exact level population in $n = 62$ is very sensitive on temperature and dielectronic recombination. The value given by Walmsley & Watson (1982, their Fig. 3) is $b = 0.5$, relative to LTE, implying a C62 α contribution of 0.3 Jy, which should be detectable by the CBI¹³. Lowering T_e to 50 K brings the predicted RRL flux down to 3 σ_{RRL} , i.e. marginally consistent with the CBI upper limit.

7.3 Mopra limits on K- and W-band RRLs

The detection of the RRL system of ρ Oph W in the C I model of Sec 6.3 would be very difficult. The ensemble of clumps is optically thick below $\sim 10 \text{ GHz}$. At higher frequencies the excited energy levels leading to the emission of α photons are severely depopulated relative to LTE (Salem & Brocklehurst 1979; Walmsley & Watson 1982).

We nonetheless attempted to detect the RRL system of ρ Oph W using the UNSW-MOPS spectrometer (Sec. 3.3.2), and found no RRLs at the expected radial velocity, $V_{\text{lsr}} = +3 \text{ km s}^{-1}$ (Brown & Knapp 1974; Pankonin & Walmsley 1978). With the line profiles observed at lower frequencies, of 1.5 km s^{-1} FWHM, we can estimate the expected contribution of RRLs in the Mopra datacubes and place upper limits on the high frequency RRLs.

The ensemble of C II clumps subtends a solid angle of less than $\Omega_c = \pi 1.5^2 \text{ arcmin}^2$. If there are $N_c = 30$ clumps spread uniformly over $20 \times 20 \text{ arcmin}^2$, then only one clump is expected on average in each 5 arcmin pixel. The expected intensity from one clump, covering about $\pi 8^2 \text{ arcsec}^2$ is diluted in $5 \times 5 \text{ arcmin}^2$. At $T_e = 150 \text{ K}$, the emergent peak LTE intensity in C73 α from one clump is 1262 MJy sr^{-1} , or

2.97 MJy sr^{-1} when diluted in the 5 arcmin pixels. In dense and cold gas dielectronic recombination enhances the LTE departure coefficients to $b \sim 1$. Thus with a 3 σ upper limit of 1.1 MJy sr^{-1} on C73 α , the Mopra data rule out ‘warm’ temperatures (note that collisionally excited lines, such as [C II] 158 μm , are biased towards higher temperatures). By contrast, at $T_e = 20 \text{ K}$, the peak LTE RRL intensity in 5 arcmin pixels is 0.38 MJy sr^{-1} , and $b \sim 0.3$, so that the expected C73 α intensity is only 0.12 MJy sr^{-1} - consistent with its non-detection.

In the W band the b coefficients are vanishingly small at 20 K temperatures. For C42 α and $T_e = 20 \text{ K}$, we approximate to the $n = 50$ case of Salem & Brocklehurst (1979) (for $\log(N_e / 1 \text{ cm}^{-3}) = 2.5$ and with a 100 K background): $b = 5 \cdot 10^{-4}$. The expected C42 α intensity in the 5 arcmin pixels is $b \times 9.6 \text{ MJy sr}^{-1}$, while the rms noise is 188 MJy sr^{-1} .

8 DISCUSSION

The [C II] $\lambda 158 \mu\text{m}$ image of ρ Oph A by Yui et al. (1993), with a 15 arcmin beam, shows that C⁺ is present and that [C II] $\lambda 158 \mu\text{m}$ shares a similar extent as the cm-wave continuum. It is remarkable that S 1 is not coincident with a [C II] $\lambda 158 \mu\text{m}$ peak. In this Section we discuss the likely emission levels of C I continuum in the ρ Oph environment, and consider the possibility of combining both C I and spinning dust.

8.1 Exciting stars

8.1.1 HD147889

Atmospheric parameters for the two components of HD147889 were obtained by fitting ‘‘Tlusty’’ non-LTE model atmospheres (Lanz & Hubeny 2007) to the FEROS spectra (Sec. 3.3.1), with rotation velocities $v \sin i$ of 50 and 30 km s^{-1} respectively, and a surface area ratio of 1.3. The temperatures are 23000 and 20000 K and the surface gravity $\log(g)$ is 4.25 for both components ($\log(g) < 4.0$ or > 4.5 are ruled out). The surface gravity is determined mainly from the strength of the line wings of H γ $\lambda 4340$. However, this strength also depends on the temperature. The temperature mainly comes from the strength of He I $\lambda 4387$ and $\lambda 4471$ as compared with Mg II $\lambda 4481$ and the Si III triplet $\lambda \lambda 4552, 4567, 4573$.

The heliocentric velocities of each component were +64, -99 km s^{-1} on UTC = 2006-02-07, -52 km s^{-1} , $+53 \text{ km s}^{-1}$ on UTC = 2008-05-16, and -39 km s^{-1} , $+33 \text{ km s}^{-1}$ on UTC = 2008-05-17. This gives us a systemic heliocentric velocity of -7 km s^{-1} , or a local standard of rest velocity of $+3 \text{ km s}^{-1}$ (so equal to that of the carbon RRLs), and a mass ratio of 1.3.

If the two components of HD147889 are on the main sequence, as indicated by their surface gravities, then the stellar radii and masses can be inferred by interpolating the zero-age main-sequence models of Schaller et al. (1992). We obtain radii of 3.52 and 3.10 R_{\odot} , and masses of 8.31 and 6.36 M_{\odot} . But it must be borne in mind that the IR excess of HD147889 and its interaction with the ρ Oph star forming cloud make it a likely pre-main sequence star, in the sense that it is still contracting towards the zero-age main

¹² We have cross-checked our calculations against those in Pankonin & Walmsley (1978) and Eq. 3 in Heiles et al. (1996)

¹³ We have neglected the effects of stimulated emission, accounted for in the β coefficient of Walmsley & Watson (1982, their Fig. 5), because $\beta \approx 1$ for the transitions considered here

sequence. The models of Behrend & Maeder (2001, their Table 1) show that at an age of $2.4 \cdot 10^5$ yr (so close to 10^6 yr, the approximate lifetime of dark clouds), a $12 M_{\odot}$ star would still be contracting, with a surface temperature of 22 000 K and a radius of $10.3 R_{\odot}$. To make headway the spectral types we adopt are B2IV and B3IV, but we note that we lack a precise measurement of the stellar luminosities.

The line of sight to HD147889 appears to be strongly affected by extinction from LDN 1688. The H-nucleus column density map reported in Sec. 5.1 gives $N_H = 1.13 \cdot 10^{22} \text{ cm}^{-2}$ in the direction of HD147889, or $A_V = 6.76$ using the conversion factors from Draine et al. (2003) with $R_V = 3.1$. The A_V map from Ridge et al. (2006) gives $A_V = 8.1$ at the position of HD147889. However, a comparison between the observed $B-V$ colour and that expected from the model atmospheres from Castelli (2003) gives $E(B-V) = 0.8$ (or $A_V \sim 2.5$). Yet the stellar radii inferred above require extinction values $A_V = 4.5$ to be compatible with the photometry. Hence the extinction towards HD 147889 is manifestly very structured on small scales, and requires an exceptionally large $R_V = 5.6$ or higher if HD 147889 is still contracting.

8.1.2 S 1 and SR 3

S 1 is a close binary system composed of a B4V star (Lada & Wilking 1988) and a K-type companion with a 10 mJy peak at 10 GHz (including its 2 mJy radio halo, André et al. 1988). For S 1, $T_{\text{eff}} \sim 15800$ K, and surface gravity $\log(g/\text{cm s}^{-2}) = 4.0$. The spectral type we adopt for SR 3 is B6V (Elias 1978), or $T_{\text{eff}} \sim 14000$ K, $\log(g/\text{cm s}^{-2}) = 4.0$. Lada & Wilking (1988, their Sec. IIIb) and Bontemps et al. (2001) give bolometric luminosities L_{\star} for S 1 and SR 3. For S 1, $L_{\star} = 1100 L_{\odot}$, which is consistent with B4V, but for SR 3, $L_{\star} = 100 L_{\odot}$, which is too low for B6V. The spectral type of SR 3 is probably closer to B9V.

8.2 Physical conditions

The 1.1 mm continuum data in Young et al. (2006) are strongly high-pass filtered and trace the smaller angular scales. They find an average density of $\sim 10^6 \text{ cm}^{-3}$ in 44 molecular cores containing $\sim 80 M_{\odot}$, or about 1/20–1/100 the mass of the entire ρ Oph complex (see Sec. 5.1).

A density of $n_H = 10^4 - 10^5$ is given by Liseau et al. (1999) from PDR models of the far-IR line ratios. They fit [O I] 63, 145 μm , while the [C II] 158 μm levels can only be reproduced with $n_H = 10^6 \text{ cm}^{-3}$ and an unrealistically low field G_{\circ} . Higher densities than 10^6 cm^{-3} are required to accommodate $G_{\circ} \sim 100$ inferred by Liseau et al. (1999). They treated HD147889 as a main sequence star, and used a distance of 150 pc. With the Hipparcos distance to HD147889 of 135 pc and luminosity class IV we obtain $G_{\circ} = 629$, using the model atmospheres from Castelli (2003).

Bypassing the PDR models, we can infer a H-nucleus density from the [C II] 158 μm cooling rate (e.g. Tielens 2005, his Eq. 2.67). The fluxes from Liseau et al. (1999) then give $n_H \sim 3 \cdot 10^4 - 2 \cdot 10^6 \text{ cm}^{-3}$ for temperatures of 10 – 100 K and a filling factor $f = 10^{-3}$. Note, however, that the critical density of [C II] 158 μm is $2.7 \cdot 10^3 \text{ cm}^{-3}$ at 100 K, so that it does not trace the dense clumps required by the C I continuum model.

8.3 C I Strömgrén spheres

The model atmospheres from Castelli (2003) predict that the C-ionizing luminosity of HD147889 is ~ 25 times that of S 1 and 612 times that of SR 3. From its vantage point at the back of the ρ Oph main cloud HD147889 illuminates the entire cloud (Liseau et al. 1999). By contrast S 1 is surrounded by its disk-like circumstellar nebula (which probably stems from the clumpy walls of a wind-blown cavity, see Sec. 5.1). Since S 1 is optically visible a fraction of its UV luminosity escapes. The small part of its carbon-ionising flux that is absorbed in the dense circumstellar disk radiates a meagre 2 mJy at 5 GHz (André et al. 1988).

If the C II regions of ρ Oph are ionisation-bounded nebulae their average electron density is given by ionisation balance: $n_e^2 = S/\alpha V$, where V is nebular volume and S is the stellar luminosity in C-ionising photons (below H-ionising energies). We use the total recombination coefficients α from Nahar & Pradhan (1997), assuming $T_e = 100$ K. For optically thin radiation, the total C II region flux density is

$$F_{\nu} = SB_{\nu}\kappa_{\nu}^1/\alpha, \quad (1)$$

where B_{ν} is the Planck function, and κ_{ν}^1 is the C I free-free opacity for unit electron density.

For S 1, we obtain $S = 9.9 \cdot 10^{45} \text{ s}^{-1}$, which for a closed geometry should give an integrated flux density of 458 mJy at 31 GHz. S 1 is not detected in the CBI maps. In Sec. 5.3 we report a 31 GHz point-source flux density of 1.3_{-4}^{+7} mJy for S 1. It appears that the circumstellar nebula around S 1 must be disk-like, or else sufficiently clumpy that $\sim 90\%$ of C-ionising photons escape the nebula. This is consistent with the fact that S 1 is an optically visible star (by contrast with SR 3).

For SR 3 we have $S = 4.1 \cdot 10^{44} \text{ s}^{-1}$. The predicted flux density in a closed geometry is 20 mJy at 31 GHz, consistent with its non-detection by the CBI (the 31 GHz point-source flux density of SR 3 is 2.0_{-3}^{+7} mJy).

If HD 147889 has settled on the main sequence, we find $S = 1.4 \cdot 10^{47} \text{ s}^{-1}$, and an upper limit for the 33 GHz flux density of 6.5 Jy. The background-subtracted 33 GHz flux density inside the CBI PB aperture of 45 arcmin is 6.7 Jy, of which ~ 1.5 Jy stem from the diffuse H II region surrounding HD 147889. This is close to the levels required for an ionisation bounded and spherical nebula. But part of the C-ionising radiation should escape the nebula. Thus for the C I continuum interpretation it is necessary that HD 147889 be a pre-main sequence binary star that is still contracting, with a primary stellar radius of about $4.5 R_{\odot}$, and a mass of $\sim 10 M_{\odot}$, so that $\log(g) \sim 4$ to 4.5 (as inferred from the FEROS spectroscopy), and a secondary mass of $7.7 M_{\odot}$.

The C II Stromgrén sphere around HD 147889 extends out to ~ 10 arcmin, the projected distance to ρ Oph W. For a filled sphere, the required electron density is $\sim 100 \text{ cm}^{-3}$, implying H-nucleus densities of $\sim 10^6 \text{ cm}^{-3}$. Such a C II region would be optically thin at 5 GHz and reach ~ 10 Jy, which is ruled out by the data. Thus the C II region around HD 147889 must be a thin shell, as indicated by the geometry of ρ Oph W. However, in order to reach the densities required by the SED model of Fig. 6, the thickness of the ρ Oph W C II region should be only 2–3 arcsec, which is surprisingly thin. Such a thin shell could be replaced by an ensemble of flat clumps seen edge-on (see Sec. 6.3).

We have modelled the C II regions in ρ Oph using the Cloudy photoionisation package (version c07.02.01, last described by Ferland et al. 1998). We treat ρ Oph W as a shell in an open geometry, separated from HD147889 by its projected distance, while S 1 and SR 3 are embedded in ionisation-bounded circumstellar nebulae, with a fiducial inner radius of 10^{15} cm. The predicted C II layer in ρ Oph W is extremely narrow, with a width $\delta < 1.2$ arcsec at densities $> 10^6$ cm $^{-3}$, which is consistent with the thin ridge model. The solid angle subtended by the C II region in ρ Oph W, which consists of an ensemble of $N_c = 30$ sheets, each 3.7 arcmin long, is about $30 \times 3.7 \times \delta/60$ arcmin 2 . This is a factor of ~ 100 larger than in the C II regions around S 1 and SR 3 (if the H-nucleus density is constant at 10^6 cm $^{-3}$).

8.4 Origin of the 2MASS diffuse emission

The 2MASS K_s band emission from ρ Oph W is coincident with the 31 GHz ridge. What is the nature of the nebulosity seen in the 2MASS J, H, and K_s images? All three 2MASS bands share a similar morphology with the IRAC images, although not exactly coincident.

8.4.1 Problems with near-IR scattered light, VSG continuum, and free-free

We estimated that the diffuse intensities in ρ Oph W drop at shorter wavelengths, in ratios J:H:K $\sim 1 : 2.2 : 2.7^{14}$. This is at odds with the colours expected from scattered light. Paodan et al. (2006) calculate that the emergent intensities of scattered light in neutral clouds should increase by a factor 4 from K to J. These ratios are unlikely to be affected by extinction. The interstellar extinction towards ρ Oph, excluding intra-nebular extinction, can be estimated from the value of the colour excess $E(B-V)$ in the maps of Schlegel et al. (1998). Near ρ Oph but outside any dust clouds extinction is very low, $A_V < 0.1$, as expected for Gould belt clouds, which raises the J band intensities by a meagre 3%.

On the other hand, even at 150 K the C I continuum is cut off by its Wien tail above $\sim 5 \mu\text{m}$, and is ~ 30 times fainter than the $8 \mu\text{m}$ nebulosity seen in the IRAC 4 image at $8 \mu\text{m}$. It is unlikely that the 2MASS images trace a 1000 K C^+ plasma because the solid angle of ρ Oph W in the K-band image is about 5 arcmin 2 , which would give an optically thick continuum of $\sim 10^4$ Jy at 5 GHz 15 .

Is it possible that the near-IR continuum stems from a VSG population sharing a similar morphology as the PAHs that emit in the IRAC bands? We note that the circumstellar nebulae around S 1 and SR 3 are also seen in the 2MASS K_s -band images, with JHK colours as for ρ Oph W and discrepant from that of scattered light. Sublimation dust temperatures of ~ 1000 K are required to explain the S 1

¹⁴ we used the zero points for the Montage mosaics, took the median intensity values in a square box 20 pixels on a side, centred on J2000 16:25:57.88 -24:21:11.7, and subtracted a median background extracted from a similar box but centred on J2000 16:25:58.10 -24:14:42.4

¹⁵ note, however, that the the faint continuum from the diffuse H II region about HD147889 is at ~ 7000 K and present in the K-band

Table 3. *Spitzer* IRS H₂ line intensities in W m $^{-2}$ sr $^{-1}$.

	ρ Oph W	SR 3	S 1	S 1 off
H ₂ (0-0)S(1)	3.66(-7) ^a	1.55(-7)		
H ₂ (0-0)S(2)	2.94(-7)	1.86(-7)	< 1.02(-8)	< 2.75(-9)

^a The power of ten exponent is indicated in parentheses.

and SR 3 nebulae in terms of large dust grains. So it is likely that the same VSGs that would account for the ρ Oph W near-IR emission would also be found in S 1 and SR 3. We return to the discussion on spinning dust in Sec. 5.3.

8.4.2 Rovibrational H₂

An interesting alternative to the VSG continuum is the possibility that the J, H, and K-band emission in ρ Oph W stems from H₂ rovibrational lines. Habart et al. (2003, their Fig. 2) present a (1-0)S(1) H₂ image, in which it may be appreciated that ρ Oph W is slightly offset by ~ 10 – 20 arcsec to the S-E compared to the ISOCAM PAH emission in the LW2 filter (5 – $8.5 \mu\text{m}$). There is also a hint of a shift in Fig. 5 between 2MASS K_s -band and IRAC $8 \mu\text{m}$, which may be explained if 2MASS K_s is mostly due to rovibrational H₂ and IRAC $8 \mu\text{m}$ to PAHs. Here we use the *Spitzer* spectroscopy to further investigate relationships between H₂, PAHs, and 31 GHz.

The IRS data on ρ Oph W allows estimating the intensity of the pure rotational lines H₂ S(1) and S(2), in the same manner as used in Sec. 5.3 for the PAH $11.3 \mu\text{m}$ band. Table 3 lists the H₂ line fluxes in the spectra we analysed. They are consistent with Table 1 of Habart et al. (2003).

A tentative correlation between the H₂ fluxes and 31 GHz intensities can be inferred from a comparison between Table 3 and Table 2. Note that in the specific case of SR 3, the 31 GHz intensity towards SR 3 should be $1.4 \pm 0.2(-1)$, as measured in the 31 GHz image, and not as tabulated in Table 2 (where we are testing for 31 GHz counterparts to the mid-IR compact source around SR 3). H₂ is weak or undetected in the positions of low 31 GHz intensities (i.e. S 1 and S 1 off), despite the coincidence with the peak mid- and far-IR intensities, while H₂ is bright at the 31 GHz peak (i.e. on ρ Oph W) and in SR 3. The H₂ lines are undetected towards S 1. The values reported in Table 3 for S 1 and S 1off are upper limits derived from formally extracting the H₂ line flux, despite the absence of visible lines.

In the molecular layers of PDRs the C-ionising UV radiation also excites the electronic states of H₂, which then decay in a rovibrational cascade leading to the observed near-IR fluorescent lines. The conditions in ρ Oph W are very similar to those found in NGC 2023. Black & van Dishoeck (1987) reproduce the near-IR H₂ line system of NGC 2023 with an incident UV specific intensity field of $I_{UV} = 1240$ in units of the 1000\AA UV background at the solar neighbourhood. For ρ Oph W we find that $I_{UV} = 545$, if HD147889 is on the main-sequence, or higher if it is still contracting. The more recent models of Habart et al. (2003) demonstrate that the near-IR H₂ lines in ρ Oph W are fluorescent.

Therefore in the C I model we expect that the 31 GHz continuum be coincident with fluorescent H₂. The 2MASS-

CBI match in ρ Oph W could then be explained if the 2MASS filters are dominated by H_2 line emission.

Given the $\text{H}_2(1-0)\text{S}(1)$ intensity map of Habart et al. (2003), we estimate that ro-vibrational H_2 accounts for all of the diffuse 2MASS K_s flux seen in ρ Oph W. $\text{H}_2(1-0)\text{S}(1)$, on its own, accounts for 20% of the 2MASS K_s -band specific intensities. The exact contribution is difficult to estimate because the diffuse nebosity in 2MASS is at a very low level. The noise in 2MASS K_s is 0.35 MJy sr^{-1} , while the peak intensities above background in ρ Oph W are $\sim 1 \text{ MJy sr}^{-1}$. The $\text{H}_2(1-0)\text{S}(1)$ line, if diluted in the K_s filter, corresponds to intensities of 0.2 MJy sr^{-1} (using the $\text{H}_2(1-0)\text{S}(1)$ image in Habart et al. 2003, their Fig. 2). Table 3 from Black & van Dishoeck (1987) allows to estimate that $\text{H}_2(1-0)\text{S}(1)$ represents 21.8% of the total H_2 contribution in the 2MASS K_s filter. Therefore H_2 ro-vibrational emission can account for the entire 2MASS K_s band flux.

8.5 Both C I and spinning dust?

This work focusses on the 31 GHz continuum as seen by the CBI. Yet inspection of the *WMAP* Ka map reveals that the entire ρ Oph cloud is outlined at 33 GHz, albeit at $\sim 1/3$ the intensities in ρ Oph W. In particular the eastern filamentary extensions of ρ Oph, LDN 1729 and LDN 1712, at 0.03 MJy sr^{-1} and $0.016 \text{ MJy sr}^{-1}$, are not detected in the 2.3 GHz map of Baart et al. (1980, in which no region of ρ Oph has a counterpart). The diffuse emission surrounding our 45 arcmin centred on ρ Oph W, also appears to have a positive spectral index between 2.3 GHz and 33 GHz $\alpha_{2.3}^{33}$. If we correct for a diffuse background at 0.03 MJy sr^{-1} , the *WMAP* 33 GHz flux density inside the CBI PB aperture drops from 14 Jy to ~ 9 Jy.

C I can better accomodate a reduced 33 GHz flux density, since the 2.3 GHz – 33 GHz rise is shallower ($\alpha_{2.3}^{33}$ drops from 0.69 to 0.52). But what is the origin of the background? The first possibility that springs to mind is spinning dust, which does not require an ionisation source, and scales linearly with density. We could also envision an ensemble of C I-emitting dense clumps illuminated by the general interstellar UV field. In this case the specific intensity in the optically thin regime at 33 GHz can be written

$$I_\nu = fLn_{C^+}n_e B_\nu \kappa_\nu^1, \quad (2)$$

where L is the depth of the ρ Oph cloud, f is the filling factor, and κ_ν^1 is as in Eq. 1. An upper limit to the product $n_{C^+}n_e$ can be obtained by ionisation balance in ionisation-bounded clumps

$$Aln_{C^+}n_e\alpha < s_C A, \quad (3)$$

for clumps with depth l and area A , where

$$s_C = \int_{\lambda_C}^{\lambda_H} d\lambda \lambda \pi J_\lambda / (hc), \quad (4)$$

is the flux of C-ionising photons per unit area in the interstellar radiation field J_λ . If $fL \approx l$, the depth of a single clump, then we have an upper limit to any C I continuum diffuse background intensity

$$I_\nu^u = B_\nu \kappa_\nu^1 s_C / \alpha. \quad (5)$$

The interstellar radiation field of Mathis et al. (1983) gives

$I_\nu^u = 0.4 \text{ MJy sr}^{-1}$, which is satisfyingly a factor of four above the observed values in ρ Oph. As in the case of ρ Oph W (Sec. 6), we require beam-diluted optically thick clumps covering a solid angle of $\sim \Omega_{\text{beam}} T_{\text{rms}} / T_e$. Thus to explain the absence of ρ Oph in Baart et al. (1980) with a noise of ~ 30 mK and a beam of 20 arcmin FWHM, the projected linear size of the clump ensemble should be < 1 arcmin, if $T_e \sim 100$ K. In ρ Oph W such narrow dimensions could perhaps be interpreted as a very narrow C II shell around HD 147889. But for the diffuse emission such a geometry seems very contrived.

9 CONCLUSION

We have found that the well-studied and nearby molecular cloud ρ Oph is surprisingly bright at 31 GHz, or ~ 1 cm wavelengths. The most conspicuous feature revealed by the CBI data is the ρ Oph W PDR.

Comparison with *WMAP* images shows that the cm-emission is not the Rayleigh-Jeans tail of the sub-mm emitting dust. Bulk dust properties are inferred from new *ISO-LWS* parallel mode data. Archival *Spitzer* data allows quantifying PAH emission. None of the comparison images match the CBI data, except for IRAC $8 \mu\text{m}$ and 2MASS K_s , which closely follow the 31 GHz ridge along ρ Oph W. *Spitzer* IRS spectroscopy in four apertures hint at a possible correlation between 31 GHz intensity and the H_2 pure-rotational lines: the H_2 lines are detected only where 31 GHz intensities are bright (i.e. towards SR 3 and ρ Oph W, and not in the vicinity of S 1).

We considered several interpretations for the 31 GHz emission, requiring either an additional radio continuum component such as magnetic or spinning dust, or unexpected physical conditions, such as in a very dense and cold plasma. We find that both spinning dust and C I continuum can explain the data:

- Magnetic dust is discarded on morphological grounds. The expected 31 GHz intensity from a magnetic enhancement of the grain opacity is at odds with the CBI data. The polarization levels required by magnetic dust are not observed.

- Spinning dust can account for the radio spectrum. But the predicted levels in S 1 are in excess by a factor > 40 at 3σ . We take the intensities in PAH $11.3 \mu\text{m}$ as a proxy for the mid-IR VSG emission, which is approximately proportional to both the VSG column and local UV intensity U . Taking into account the range of spinning dust emissivities in all possible environments, the uncertainties in our 31 GHz map can marginally reconcile spinning dust with the data (i.e. at 3σ variations).

- Alternatively a cold plasma such as that found in C II regions could explain the 31 GHz emission. The star HD147889, a binary pre-main-sequence star with spectral types B2IV, B3IV, emits sufficient C-ionising UV radiation to interpret ρ Oph W as a C II region. But the absence of detectable < 10 GHz signal requires optically thick emission, and hence high H-nucleus densities ($n_{\text{H}} \sim 10^7 \text{ cm}^{-3}$, almost a factor of 10 higher than inferred in the literature), implying a hitherto unobserved molecular phase of the ISM. In ρ Oph this molecular phase takes the form of an ensemble of dense clumps or sheets at temperatures of order 50 K or

less. The cold plasma interpretation explains the 2MASS - CBI correlation through an important fluorescent H₂ contribution to the 2MASS bands.

ACKNOWLEDGMENTS

We thank the referee for a thorough reading and useful comments. S.C. acknowledges support from FONDECYT grant 1060827, and from the Chilean Center for Astrophysics FONDAP 15010003. We gratefully acknowledge the generous support of Maxine and Ronald Linde, Cecil and Sally Drinkward, Barbara and Stanely Rawn, Jr., Fred Kavli, and Rochus Vogt. This work was supported by the National Science Foundation under grants AST 00-98734 and AST 02-06416. RP acknowledges the support of a Spitzer Cycle-5 archival proposal grant (PAC.PALADINI - 1 - JPL.000094). This publication makes use of data products from 1- the Two Micron All Sky Survey, which is a joint project of the University of Massachusetts and the Infrared Processing and Analysis Center, funded by the National Aeronautics and Space Administration and the National Science Foundation, and 2- the Southern H-Alpha Sky Survey Atlas (SHASSA), which is supported by the National Science Foundation. The Mopra radio telescope is part of the Australia Telescope which is funded by the Commonwealth of Australia for operations as a National Facility operated by CSIRO. This research also made use of Montage, funded by the National Aeronautics and Space Administration's Earth Science Technology Office, Computational Technologies Project, under Cooperative Agreement Number NCC5-626 between NASA and the California Institute of Technology. The code is maintained by the NASA/IPAC Infrared Science Archive. This research has made use of the SIMBAD database, operated at CDS, Strasbourg, France.

REFERENCES

- André, P., Montmerle, T., Feigelson, E. D., Stine, P. C., & Klein, K.-L. 1988, *ApJ*, 335, 940
- Abergel, A., et al., 1996, *A&A*, 315, L329.
- Baart, E.E., de Jager, G., Mountfort, P.I., *A&A*, 1980, 92, 156.
- Barsony, M., Kenyon, S. J., Lada, E. A., & Teuben, P. J. 1997, *ApJS*, 112, 109
- Behrend, R., Maeder, A., 2001, *A&A*, 373, 190
- Bennett, C. L., Halpern, M., Hinshaw, G., Jarosik, N., Kogut, A., Limon, M., Meyer, S. S., Page, L., Spergel, D. N., Tucker, G. S., Wollack, E., Wright, E. L., Barnes, C., Greason, M. R., Hill, R. S., Komatsu, E., Nolte, M. R., Odegard, N., Peiris, H. V., Verde, L., Weiland, J. L., 2003, *ApJSS*, 148, 1
- Bernard, J.P., Boulanger, F., Puget, J.L., 1993, *A&A* 277, 609.
- Berné et al. 2007, *A&A*, 469, 575
- Black, J.H., van Dishoeck, E.F., 1987, *ApJ*, 322, 412
- Bontemps, S., et al., *A&A*, 372, 173.
- Boulanger, F., Perault, M., 1988, *ApJ*, 330, 964
- Boulanger, F., et al., 1996, *A&A*, 315, L325.
- Brown, R.L., Knapp, G.R., 1974, *ApJ*, 189, 253
- Calabretta, M.R., 1991, *AuJPh*, 44, 441
- Casassus, S., Readhead, A.C.S., Pearson, T.J., Nyman, L.-Å, Shepherd, M.C., Bronfman, L., 2004, *ApJ*, 603, 599
- Casassus, S., Cabrera, G. F., Förster, F., Pearson, T. J., Readhead, A. C. S., Dickinson, C., 2006, *ApJ*, 639, 951
- Casassus, S., Nyman, L.-Å., Dickinson, C., Pearson, T. J., 2007, *MNRAS*, 382, 1607
- Cartwright, J. K., Pearson, T. J., Readhead, A. C. S., Shepherd, M. C., Sievers, J. L., Taylor, G. B., 2005, *ApJ*, 623, 11
- Castelli, F., Kurucz, R. L., 2003, *IAU symp.* 210, A20.
- Chan, S. J., et al., 2001, in 'The Calibration Legacy of the ISO Mission'. Eds. L. Metcalfe & M.F. Kessler, ESA SP-481
- Chrysostomou, A., Clark, S. G., Hough, J. H., Gledhill, T. M., McCall, A., Tamura, M., 1996, *MNRAS*, 278, 449
- Condon, J.J., Griffith, M.R. & Wright, A.E., 1993, *AJ*, 106, 1095
- Dickinson C., Casassus S., Pineda J. L., Pearson T. J., Readhead A. C. S., Davies R. D., 2006, *ApJ*, 643, L111
- Dickinson, C., Davies, R. D.; Davis, R. J., 2003, *MNRAS*, 341, 369
- Draine, B., 2003, *ARAA*, 41, 241
- Draine, B. T., Bertoldi, F., 1996, *ApJ*, 468, 269.
- Draine, B.T., Lazarian, A., 1998a, *ApJL*, 494, L19
- Draine, B.T., Lazarian, A., 1998b, *ApJ*, 508, 157
- Draine, B.T., Lazarian, A., 1999, *ApJ* 512, 740
- Draine, B.T., Lazarian, A., 1999, 'Microwave Foregrounds', ASP Conference Series, Vol. 181, A. de Oliveira-Costa and M. Tegmark, eds.
- Draine, B.T., Li, A., 2001, *ApJ*, 551, 807
- Draine, B.T., Li, A., 2007, *ApJ*, 657, 810
- Dupac, X., et al., 2003, *A&A*, 404, L11.
- Elias, J.H., *ApJ*, 1978, 224, 453
- Encrenaz, P.J., 1974, *ApJL*, 189, 135
- Falgarone, E., Gilmore, W., 1981, *A&A*, 95, 32
- Ferland, G. J. Korista, K.T. Verner, D.A. Ferguson, J.W. Kingdon, J.B. Verner, & E.M. 1998, *PASP*, 110, 761
- Finkbeiner, D.P., Schlegel, D.J., Frank, C., Heiles, C., 2002, *ApJ*, 566, 898
- Finkbeiner, D.P., 2004, *ApJ*, 614, 186,
- Gagné, M., Skinner, S.L., Daniel, K. J., 2004, *ApJ*, 613, 393
- García Lario, P., 2001, SAI/2001-030/Rp. Version 1.0.
- Gaustad, J. E., McCullough, P. R., Rosing, W., Van Buren, D., 2001, *PASP*, 113, 1326
- Grasdalen, G., Strom, K.M., Strom, S.E., 1973, *ApJL*, 184, 53
- Hafner, L.M., Meyer, D.M., 1995, *ApJ*, 453, 450
- Habart, E., Boulanger, F., Verstraete, L., Pineau des Forêts, G., Falgarone, E., Abergel, A., 2003, *A&A*, 397, 623
- Heiles, C., Bon-Chul, K., Levenson, N.A., Reach, W.T., 1996, *ApJ*, 462, 326
- Hinshaw, G., et al., 2007, *ApJS*, 170, 288
- Habing, H. J., 1968, *Bull. Astr. Inst. Netherlands.*, 19, 421
- Houk, N., Smith-Moore, M., 1988, Michigan Spectral Survey, Ann Arbor, Dept. of Astronomy, Univ. Michigan (Vol. 4)
- Iglesias-Groth, S., 2005, *ApJ*, 632, 25.
- Iglesias-Groth, S., 2006, *MNRAS*, 368, 1925.
- Lanz, T., Hubeny, I. 2007, *ApJS*, 169, 83.
- Leitch, E.M., Readhead, A.C.S., Pearson, T.J., Myers,

- S.T., 1997, ApJL 486, L23
 Lada, C.J., Wilking, B.A., 1988, ApJ, 287, 610.
 Liseau, R., Lorenzetti, D., Molinari, S., et al., 1995, A&A, 300, 493.
 Liseau, R., et al., 1999, A&A, 344, 342.
 Lockman, F.J., Pisano, D.J., Howard, G.J., 1996, ApJ, 472, 173
 Lynds, B.T., 1962, ApJS, 7, 1
 Martin, P.G., 2007, EAS Publications Series, 23, 165.
 Mathis, J.S., Mezger, P.G., Panagia, N., 1983, A&A, 128, 212
 Miville-Deschenes., M., Lagache, G., 2005, ApJS, 157, 302.
 Nahar, S.N., Pradhan, A.K., 1997, ApJSS, 111, 339.
 Padgett, D. L., et al., 2008, ApJ, 672, 1013.
 Padin, S., et al, 2002, PASP, 114, 83
 Padoan P., Juvella M., Pelkonen V.-M., 2006, ApJ, 636, 101
 Pankonin, V., Walmsley, C.M., 1978, A&A, 64, 333.
 Readhead, A. C. S., et al., 2004, Science, 306, 836
 Reich, W., Fuerst, E., Reich, P., Reif, K., 1990, A&AS, 85, 633
 Ridge, N.A., et al., 2006, AJ, 131, 2921.
 Salem, M., Brocklehurst, M., 1979, ApJS, 39, 633.
 Schaller, G., Schaerer, D., Meynet, G., Maeder, A., 1992, A&AS, 96, 269
 Shepherd, M.C., 1997, in Astronomical Data Analysis Software and Systems VI, ed. G Hunt & H.E. Payne, ASP conference series, v125, 77-84 “Difmap: an interactive program for synthesis imaging”.
 Schlegel, D.J., Finkbeiner, D. P., Davis, M., 1998, ApJ, 500, 525
 Smith, J. D. T., Dale, D. A., Armus, L., et al. 2004, ApJS, 154, 199
 Stutzki, J., Bensch, F., Heithausen, A., Ossenkopfm V., Zielinsky, M., 1998, A&A, 336, 697.
 Tielens, A.G.G.M., 2005, “The Physics and Chemistry of the Interstellar Medium”, ISBN 0521826349. Cambridge, UK: Cambridge University Press.
 Walmsley, C.M., Watson, W.D., 1982, ApJ, 260, 317.
 Webster, A., 1992, MNRAS, 255, 41
 Wheelock, et al., 1991, IRAS Sky Survey Atlas Explanatory Supplement..
 Witt, A.N., Gordon, K.D., Furton, D.G., 1998, ApJL, 501, 111
 Wootten, A., Snell, R., Glassgold, A. E., 1979, ApJ, 234, 876
 Wootten, A., Evans, N. J., II, Snell, R., vanden Bout, P, 1978, ApJL, 225, 143
 Young, K.E., et al., 2006, ApJ, 644, 326
 Yui, Y.Y., Nakawaga, T., Doi, Y., Okuda, H., Shibai, H., Nishimura, T., Low, F., 1993, ApJ, 419, L37.

APPENDIX A: IMAGE RECONSTRUCTION

Image reconstruction from interferometer data is an instance of the inverse problem. The compact configuration of the CBI interferometer results in the (u, v) coverage shown in Fig. A1. Missing spacings and noise impose non-linear deconvolution methods. With a uniform grid the number of free parameters (here 256^2) can exceed the number of independent data points, so that the fit is degenerate. In this case we take as a measure of the quality of fit χ^2/f , where

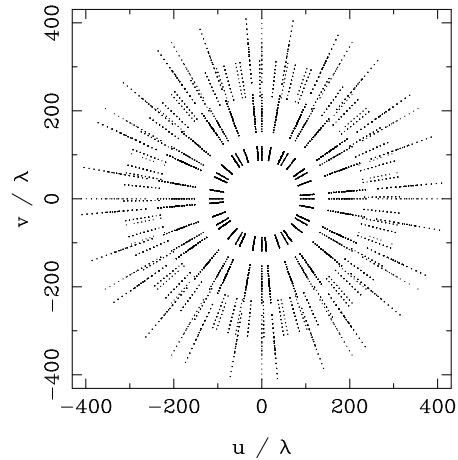


Figure A1. (u, v) coverage of the CBI in the compact configuration used for the observations of ρ Oph W.

f is the number of independent data points. χ^2/f should be close to 1 for a satisfactory model. The first few conjugate gradient iterations in the least-squares algorithm fit the bulk of the signal, but inevitably converge on noisy models, with χ^2/f values much less than 1. MEM regularization prevents the models from fitting the noise. The model shown in Fig. 1 has $\chi^2/f = 1.20$, which is somewhat high, but reconcilable with 1.0 through a 10% increase in the noise. The noise in each visibility point is calculated as the root-mean-square (rms) scatter of ~ 120 samples, and does not include residual errors in calibration, which may perhaps amount to 10%.

A reconstruction starting from a blank image as initial condition, rather than the image prior M_i , converges on essentially the same model as Fig. 1, but with a higher $\chi^2/f = 1.4$, and thus larger residuals. The prior we chose accounts for some of the extended emission seen by *WMAP*, but keeps the IRAC resolution by replacing the emission within the CBI primary beam with the IRAC $8 \mu\text{m}$ image, suitably scaled and processed so as to resemble the blank-prior MEM models (i.e. we patched-out stellar features, namely S 1 and SR 3, see below). This patched image was then fed as initial condition and prior into a sky-plane MEM deconvolution of the *WMAP* Ka image, producing the prior image used for the CBI reconstructions in Fig. 1, with $\chi^2/f = 1.2$.

The CBI observations and the quality of the MEM model can be examined through the restored image and the residuals shown on Fig. A2a, A2b. The residual image is the dirty map (produced with the DIFMAP package using natural weights, Shepherd 1997), of the residual visibilities (the difference between the observed and model visibilities). The restored image is the sum of the residual image, after division by the CBI primary beam, and the MEM model convolved with an elliptical Gaussian fit to the natural-weight synthetic beam ($8.17 \times 7.99 \text{ arcmin}^2$). In natural weights the theoretical rms noise of the dirty map is $3.4 \text{ mJy beam}^{-1}$. The dynamic range of the restored image shown in Fig. A2 is of order 100.

We examined the statistical properties of the MEM reconstructions with the simulations described in Appendix B

of Casassus et al. (2006). These simulations are relevant to assess the effects of the CBI beam on the morphological analysis of Sec. 4.1, and to estimate the dynamic range of the MEM reconstructions. The CBI MEM prior is a suitable template. We ran the same MEM algorithm as applied to the CBI visibilities on a simulation of CBI observations on the prior used for the reconstruction of Fig. 1. Fig. A2 compares this prior image with the average and dispersion of the MEM models run on 90 realisations of complex visibility noise. Note that in this case we used a blank prior with $\lambda = 20$ and $M_i = 0.3 \text{ Jy sr}^{-1}$. The 31 GHz model image obtained with this MEM reconstruction is shown in Fig. A2d. It is very similar to Fig. 1. We take this similarity as a proof of robustness of the MEM reconstructions, and also as ground to extrapolate the dynamic range of the simulations, of ~ 20 , to the CBI images.

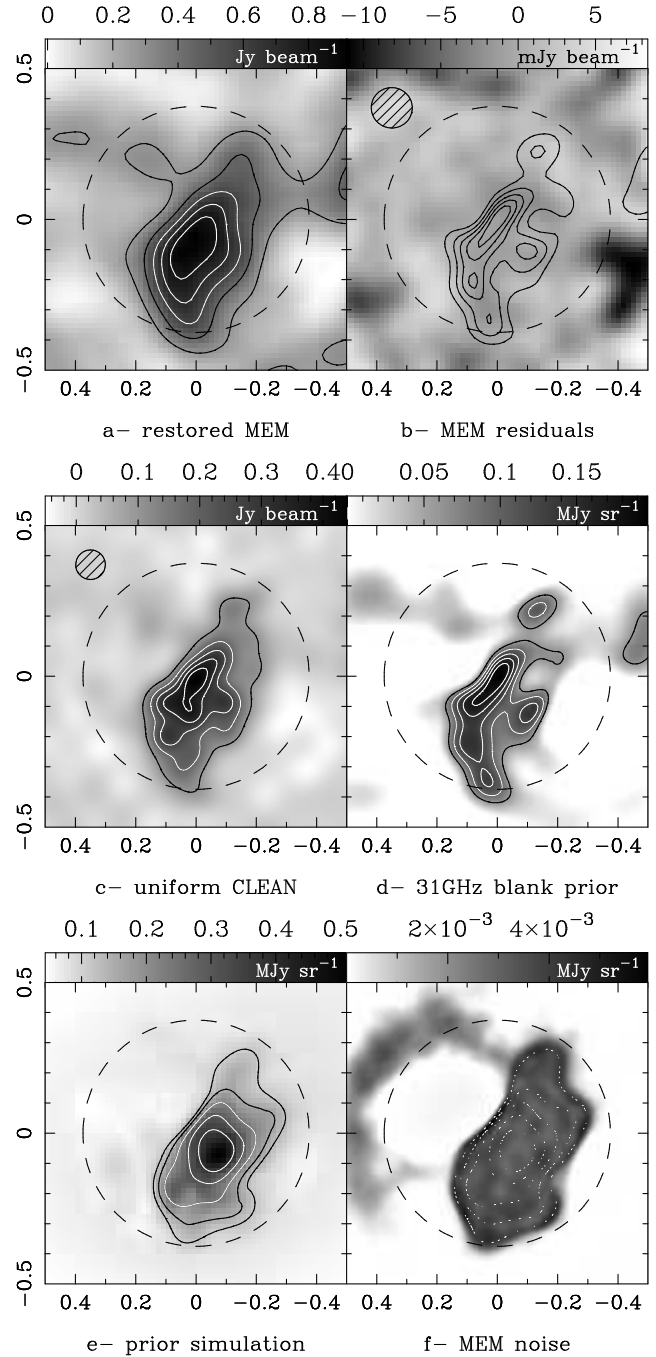


Figure A2. MEM restored image and comparison reconstructions. The axes and dashed circle follow from Fig. 1. **a-** restored image, with contour levels at 0.012, 0.286, 0.446, 0.581, 0.702 and 0.813 Jy beam^{-1} , and peak at 0.916 Jy beam^{-1} . **b-** MEM contours overlaid on the residual image. The natural-weight synthetic beam is indicated by the hatched ellipse. **c-** DIFMAP CLEAN reconstruction of the CBI data, in uniform weights. Contour levels are 0.098, 0.185, 0.257, 0.323 and 0.382 Jy beam^{-1} . **d-** A CBI MEM model with a blank prior is shown in grey scale, with contours at 0.06, 0.09, 0.12, 0.15 and 0.17 MJy sr^{-1} . **e-** average MEM model of CBI simulations on the prior image used to produce our best model. Contours are at 0.098, 0.185, 0.257, 0.323, 0.382 MJy sr^{-1} , overlaid on a grey scale of the input image. **f-** averaged MEM contours overlaid on the root-mean-square (rms) dispersion of the MEM models.